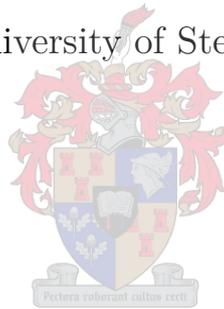# Computing the Arnold Tongue in the Zipoy-Voorhees Space-time

by

Abbas Mohamed Sherif

Thesis presented in partial fulfilment of the requirements for the degree
Master of Science in the Faculty of Science at the
University of Stellenbosch

Supervisor: Dr. Jeandrew Brink
Co-supervisor: Prof. Frederik G. Scholtz
Faculty of Science
Department of Physics

March 2017

Declaration

By submitting this thesis electronically, I declare that the entirety of the work contained therein is my own, original work, that I am the sole author thereof (save to the extent explicitly otherwise stated), that reproduction and publication thereof by Stellenbosch University will not infringe any third party rights and that I have not previously in its entirety or in part submitted it for obtaining any qualification.

Signature: _____ Abbas M. Sherif _____

Abstract

In this thesis I study the integrability of the geodesic equations of the Zipoy-Voorhees metric. The Zipoy-Voorhees spacetime is a one parameter family of Stationary Axisymmetric Vacuum spacetimes (SAV's) that is an exact solution to the vacuum Einstein Field Equations (EFE's). It has been conjectured that the end state of any asymptotically flat black hole formed by astrophysical mechanisms, such as for example, gravitational collapse of a star, merger of two black holes etc will be a characterised by the Kerr metric. The black hole will thus be a possibly rotating, stationary axisymmetric vacuum spacetime characterised by its mass and spin and will possess no closed time-like curves. Investigating orbits in the Zipoy-Voorhees spacetime serves as a concrete example to of how the Kerr hypothesis fails. For this metric, I compute the Poincaré map and then compute the rotation curve. The Poincaré map is a tool to locate the region where chaos occurs in a dynamical system. The rotation curve is used to quantify chaos in the system. I focus my study on the 2/3 resonance for a range of the parameter values $\delta \in [1, 2]$. The value $\delta = 1$ corresponds to the Schwarzschild solution where the system is integrable. I then compute the Arnold tongue by plotting the size of the resonant regions against the parameter values to quantify the departure from integrability. I find that the shape of the tongue of instability is nonlinear and the Arnold tongue pinches off at $\delta = 1.6$.

Keywords. *Curvature, Invariants, Geodesics, Spacetime, Rotation curve, Poincaré map, Resonance, Arnold tongue.*

Opsomming

In hierdie tesis bestudeer ek die integreerbaarheid van die geodesiese vergelykings van die Zipoy-Voorhees metrieke. Die Zipoy-Voorhees ruimtetyd is 'n familie van stilstaande axisimmetriese vakuum ruimtetye (SAV's) wat 'n presiese oplossing vir die vakuum Einstein veldvergelykings (EFE se). Dit is veronderstel dat die einde toestand van enige asimptotiese plat gravitasiekolk wat gevorm word deur astrofisiese meganismes, soos byvoorbeeld, gravitasie ineenstorting van 'n ster, samesmelting van twee swart gate ens sal 'n gekenmerk word deur die Kerr metrieke. Die gravitasiekolk sal dus 'n moontlik roterende, stilstaande axisimmetriese vakuum ruimtetyd gekenmerk deur die massa en spin en sal geen geslote tyd-agtige kurwes besit nie. Die studie van trajekte in die Zipoy-Voorhees ruimtetyd dien as 'n konkrete voorbeeld van hoe die Kerr hipotese versuim. Vir hierdie metrieke, ek bereken die Poincaré kaart en dan bereken die rotasie kurwe. Die Poincaré kaart is 'n instrument om die streek op te spoor waar chaos plaasvind in 'n dinamiese stelsel. Die rotasie kurwe word gebruik om chaos in die stelsel te kwantifiseer. Ek fokus my studie op die 2/3 resonansie vir 'n verskeidenheid van die parameterwaardes $\delta \in [1, 2]$. Die waarde $\delta = 1$ stem ooreen met die Schwarzschild oplossing waar die stelsel integreerbaar is. Ek bereken die Arnold tong deur die grootte van die resonante streke te plot teen die parameterwaardes om die afwyking van integreerbaarheid te kwantifiseer. Ek vind dat die vorm van die tong van onstabiliteit nielineêre is en dat die Arnold tong onverwags by 'n parameter waarde van $\delta = 1.6$ afsluit.

Sleutewoorde. *Kurwe, Invarianten, Geodesics, Ruimte-tyd, rotasie kurwe, Poincaré kaart, resonansie, Arnold tong.*

Acknowledgements

I would first and foremost like to thank my supervisor, Dr. Jeandrew Brink for her invaluable support. Not only has she directed me throughout my thesis but she exposed me on how to go about doing independent research. She was open to discussions and questions even during off schedules. She has exposed me greatly to the workings of General Relativity and stimulated my interest in numerical relativity.

My sincere thanks to the Government of Liberia for sponsoring my MSc studies without which I will not be here today.

And then to Ms. Christine Ruperti who was very helpful in providing suggestions and giving pieces of advice on my studies in general in Stellenbosch University.

Thank you also go to family and close friends who have provided moral support over the past two years. Their encouragements were needed. S. Ahmed Sherif, Sheck A. Sherif and Suliman S. Sherif are special cases worth mentioning. Thank you.

Contents

List of Figures

List of Figures 1

Chapter 1

Introduction

In a binary system if one of the objects is way more massive ($> 10^6$ times) than the other, it is called an Extreme Mass Ratio Inspiral (EMRI). Such binaries are thought to be at the centers of most galaxies. The expectation is that the more massive object is a supermassive black hole whose surrounding spacetime is nominally Kerr. Such inspirals could emit gravitational waves that are detectable by modern gravitational waves detectors such as the evolved Laser Interferometer Space Antenna (eLISA) and the New Gravitational Waves Observatory (NGO) which is sensitive to binary systems with a combined mass of the order $10^5 - 10^7 M_\odot$ [53]. Completion of the Square Kilometer Array (SKA) in 2024 would provide us with 10^4 times more survey speed and 50 times more sensitivity than the current high survey speed and high sensitivity telescopes [1]. The high sensitivity is important since this would mean that the SKA could detect many new faint pulsar signals and potentially a pulsar around the Galactic Center Sgr A*. Continued monitoring of these pulsars could aid the detection of low frequency gravitational waves [42, 71].

The purpose of this thesis is to explore ways of testing the Kerr hypothesis and quantifying departures from the Kerr spacetime. The Kerr hypothesis states that the end state of any asymptotically flat blackhole formed by astrophysical mechanisms, such as gravitational collapse of a star, merger of two blackholes etc is a

Kerr blackhole. The blackhole will thus be a possibly rotating, stationary axisymmetric vacuum spacetime characterised by its mass and spin and will possess no closed time-like curves [15, 37, 41, 73].

In [74], Ryan showed that multipole moments of the more massive object can be extracted from the gravitational waves emitted during the EMRI. In [16] Collins and Hughes constructed a perturbed blackhole which they called bumpy blackholes. The idea was to quantify the deviation in the multipole moments from Kerr. Other methods have been used to study perturbation from Kerr through gravitational waves signals [22, 26, 27, 29, 31, 43, 75]. In [25, 27, 28] the authors studied the nonlinear dynamics of the equations of motion of perturbed blackholes. They found that behaviour related to non-linear dynamics appear in the perturbed blackholes spacetime. This was due to the fact that these perturbed blackhole spacetimes were missing a fourth constant of motion analogous to the Carter constant in the Kerr spacetime [53].

I explore the integrability of the Zipoy-Voorhees spacetime [47, 87, 98] to quantify the effect of the departure from the Kerr metric on the orbits of the spacetime. The Zipoy-Voorhees spacetime is a stationary axisymmetric vacuum (SAV) spacetime constructed from the complex Ernst potential [11, 45], and is parametrized by a parameter δ. The Schwarzschild solution $\delta = 1$ is integrable, as is the Minkowski space solution $\delta = 0$. There have been studies of this spacetime to investigate its integrability [11, 53]. I briefly summarize the main findings of [53] later in the introduction. However, this thesis provides the first time the Arnold tongue has been computed for the Zipoy-Voorhees spacetime. The Arnold tongue enables us to quantify the region of numerical chaos and compute the parameter value(s) for which the spacetime is integrable.

The Zipoy-Voorhees spacetime fails the Painlevé test just as the Fokas-Lagerstrom Hamiltonian. However, this was found to be inconclusive in stating whether the spacetime is integrable since there can be a transformation of the Hamiltonian such that the transformed Hamiltonian passes the Painlevé test as was the case of the Fokas-Lagerstrom Hamiltonian [39].

J. Brink in [11] in 2008 studied the integrability of the Zipoy-Voorhees spacetime by observing the structure of orbits in configuration space. The author formulated the problem of finding the fourth first integral of the metric in addition to the Hamiltonian and the two killing vectors ∂_t and ∂_ϕ. The author showed that a large class of SAV spacetimes have orbits that appear numerically to admit a fourth order invariant but however pointed out the difficulty in fully characterizing the whole spacetime as integrable or nonintegrable due to the fact that there does not exist a systematic way to construct invariants that commute with the Hamiltonian.

In 2012 G. Lukes-Gerakopoulos numerically studied the Zipoy-Voorhees space-time and found that in general it was non-integrable [53]. The rotation number, which will also be employed in this thesis in chapter 4, was studied by Lukes-Gerakopoulos in [53] as integrability indicator. He showed that chaos is strongly correlated to the resonant tori that have been destroyed for nearly integrable Hamiltonian systems. However, as shown by Maciejewski, A. J. et al. [54], the result in Lukes-Gerakopoulus paper should be interpreted with caution. Maciejewski, A. J. et al in [54] produced a Poincaré map that was far removed from the one in [53]. This was due to the fact that Maciejewski, A. J. et al. [54] used a more precise integration scheme (in [53] he used the Runge-Kutta 5 method). This begs the question of how many results that have been published on chaos in the Zipoy-Voorhees Metric are dependent on the integrator used. In the same paper [54], the authors used an analytical approach and rigorously showed that the Zipoy-Voorhees, for the special case $\delta = 2$ does not admit a fourth first integral of a class of meromorphic functions (functions holomorphic over isolated points of the domain and the isolated points, which are singularities, are Laurent series expandable). This is a fairly large class of functions since they allowed this first integral to be singular at some isolated points of the phase space covered by the invariant tori. The authors essentially excluded not only first integral types that are polynomial in momenta but also some rational and transcendental ones. The result of [54] makes integrability unlikely but not impossible as a first integral may exist if we are to further extend the class of allowed functions over the entire domain. The authors made use of the differential Galois theory, particularly the

Morales-Ramis theorem to prove their result [10, 58].

Resonances are of interest because they can be observed during inspirals of compact objects into a super-massive blackhole. During such inspirals the evolving frequencies go through series of low order resonances where the ratio of orbital frequencies (longitudinal an orbital) is equal to the ratio of small integers. There is a theorem, the KAM theorem [6, 67], that associates low order resonant orbits with the onset of chaos when an integrable system is perturbed. For this reason I study the location of resonances (in particular the 2/3 resonance) in this thesis and quantify the nature of their impact.

This thesis is organized as follows. In chapter 2, I compute the curvature of the Zipoy-Voorhees spacetime and discuss the Petrov classification. In chapter 3, I discuss some literature of the integrability of dynamical systems (in particular Hamiltonian systems). The mathematical foundation on which these concepts are based are also explored. The concept of the Poincaré map and theorems concerning geodesics are discussed in chapter 3. In chapter 4, I discuss the effective potential of the Zipoy-Voorhees spacetime. The effective potential is used to visualize the orbits in the spacetime and to see where the orbit may plunge, stay bound in a finite region of spacetime or escape to infinity. I then explore geodesic motions in the spacetime via the use of the Poincaré maps. I use the Poincaré maps to compute the rotation number for the surfaces on the Poincaré map to look for where the 2/3 resonance occurs for the parameter value $\delta = 2$ and quantify how big this region is. In chapter 5, I first give an example, using the Mathieu equation [51], of a resonant tongue of instability [5, 70], which gives us the demarcation of the stable and unstable regions of trajectories. I then compute the Arnold tongue of the Zipoy-Voorhees spacetime. This is done by investigating the change in the size and shape of the resonant region as we decrease the parameter downward (i.e. as we move toward the Schwarzchild's case when $\delta = 1$). In chapter 6, I conclude and suggest possible research directions.

In this thesis I adopt the convention of setting the speed of light c and the gravitational constant G equal to 1.

Chapter 2

Properties of the Zipoy-Voorhees Metric

In this chapter I introduce the Zipoy-Voorhees metric and discuss some of its properties. The curvature tensor is computed and the Weyl scalars, obtained from the Weyl tensor and its contraction with some specified null frame, are used to specify the Petrov-type spacetime for a specified parameter δ value. The Petrov-type classification is useful in that it ascertains that the parameter value $\delta = 1$ recovers a type-D spacetime which is associated with gravitational fields. A perturbation away from the $\delta = 1$ case will give us an indication of how the gravitational field is changing. For example in [4], Arenda and Dotti show an example of the flow from the Schwarzschild spacetime (which is type-D) to type-II spacetime. In doing so the gravitational field changes in a highly nonlinear way. This study in [4] gives us an idea of how the gravitational field should change as we increase δ.

The Zipoy-Voorhees Spacetime is a vacuum solution to the Einstein Field Equations where $R_{\alpha\beta} = 0$. It falls in the category of spacetimes collectively known as stationary axisymmetric vacuum spacetimes (SAVS). I discuss some properties of the metric.

6

The line element is given by

$$ds^2 = -e^{2\psi}dt^2 + e^{-2(\psi-\gamma)}\left(d\rho^2 + dz^2\right) + e^{-2\psi}R^2 d\phi^2 \qquad (2.1)$$

For coordinates

$$
\begin{aligned}
x &= \cosh\left(\rho\right)\\
y &= \cos\left(z\right)
\end{aligned}
\qquad (2.2)
$$

define

$$
\begin{aligned}
e^{2\psi} &= \left(\frac{x-1}{x+1}\right)^{\delta}\\
e^{2\gamma} &= \frac{(x^2-1)^{\delta^2}}{(x^2-y^2)^{\delta^2-1}}\\
R &= \sqrt{(x^2-1)(1-y^2)}
\end{aligned}
\qquad (2.3)
$$

The prolate spheroidal coordinates (x,y) is useful in simplifying expressions of the metric components as well as other quantities computed from the metric. The pair (ρ, z) are the factor structure coordinates. The function $\mathbb{R}\left(\varrho\right) = e^{2\psi}$ in the line element of the Zipoy-Voorhees Spacetime as defined in equation (2.1) is the real part of the complex Ernst potential (ϱ). The complex potential is obtained from the Ernst equation

$$\mathbb{R}\left(\varrho\right)\overline{\nabla}^2\varrho = \overline{\nabla}\varrho.\overline{\nabla}\varrho \qquad (2.4)$$

I refer the reader to [23] for solutions to equation (2.4). The function ψ satisfies the Laplace's equation

$$\overline{\nabla}^2 \psi = 0 \tag{2.5}$$

where $\overline{\nabla} = \partial_{\rho\rho} + \frac{1}{\rho}\partial_\rho + \partial_{zz}$ and γ is determined by line integrals of ϱ. R is any harmonic function that satisfies $R_{\rho\rho} + R_{zz} = 0$ [11]. See [45,79] for more discussions on solutions to the field equations.

The quadrupole moment of the Zipoy-Voorhees metric is given by

$$Q = M^3 \delta \frac{1 - \delta^2}{3} \tag{2.6}$$

See [49]. When $\delta = 1$ we have the Schwarzschild solution and the quadrupole moment $Q = 0$. The Schwarzschild solution describes the spherically symmetric case. The value of the parameter δ describes how the spacetime deviates from Schwarzschild. For $0 < \delta < 1$ the Zipoy-Voorhees spacetime is prolate spheroidal. For the case $\delta > 1$ the spacetime is oblate spheroidal. The case for $\delta = 0$ gives the Minkowski flat spacetime.

Another property of the Zipoy-Voorhees spacetime is that it fails the "no hair theorem". The "no-hair" theorem states any blackhole spacetimes without closed-timelike curves, whose singularity obeys the cosmic censorship hypothesis and is shrouded by an event horizon, can be characterised by only its mass, spin and charge and is the Kerr metric. All higher order multipole moments can be described in terms of these three parameters. It is expected that the end stage of any astrophysical collapse is described by this Kerr metric. The Zipoy-Voorhees spacetime, however in general describes naked singularities. These are singularities that are visible to an external observer. The singularity appear along the line $\rho = 0$ for $\delta > 0$, $\delta \neq 1$.

2.1   Curvature Tensor of the Zipoy-Voorhees Spacetime

There are two frequently used methods to compute the curvature tensor. One is the direct computation using the coordinate dependent form, and the other is using the Cartan structure equations. In appendix E I discuss the formalism/theory behind these methods with references for interested readers. I compute the non-zero independent components of the curvature tensor using the structure equations as it is a convenient and less computationally expensive means of computing the curvature tensor. These are given by (in local coordinates)

$$
\begin{aligned}
R_{t\rho\rho t} &= \frac{\delta}{(x^2-1)^2}\left(\frac{x-1}{x+1}\right)^{\delta}(\delta-2x) - \delta x\left(\frac{x^2-y^2}{x^2-1}\right)^{1-2\delta^2}\left(\frac{x+1}{x-1}\right)^{\delta} \\
&\quad + \delta^2\left(\frac{x^2-y^2}{x^2-1}\right)^{2-2\delta^2}\left(\frac{x+1}{x-1}\right)^{\delta} + \delta^3 x\frac{(1-y^2)(x^2-y^2)^{1-2\delta^2}}{(x^2-1)^{2-2\delta^2}}\left(\frac{x+1}{x-1}\right)^{\delta} \\
R_{\rho\phi\phi z} &= y\left(\delta-\delta^3\right)\frac{(1-y^2)^{\frac{3}{2}}(x^2-1)^{\frac{1}{2}}}{(x^2-y^2)}\left(\frac{x+1}{x-1}\right)^{\delta} \\
R_{\phi\rho\rho\phi} &= -\left(1-y^2\right)\frac{\left(y^2+x\left(x^3+\delta-2\delta x^2+x\left(1-y^2\right)\delta^2-\delta^2+y^2\left(\delta+\delta^3\right)\right)\right)}{(x^2-y^2)} \\
&\quad \left(\frac{x+1}{x-1}\right)^{\delta} \\
R_{z\phi\phi z} &= -\frac{(x+1)^{\delta+1}}{(x^2-y^2)(x-1)^{\delta-1}}\left(x^2-y^4\left(\delta^2-1\right)-y^2\delta^2\right) \\
&\quad + \left(1-y^2\right)(x-\delta)\frac{(x+1)^{\delta-1}}{(x-1)^{\delta+1}}\left(x-x^3+\left(x^2-y^2\right)\delta-x\left(1-y^2\right)\delta^2\right) \\
R_{\rho z z\rho} &= -\frac{(x-1)^{\delta}}{2(x^2-1)(x+1)^{\delta}}\left(-2-\delta-2y^2\delta^2 x\left(x^2-\delta x-1\right)\right) \\
&\quad - \frac{(x-1)^{\delta}}{2(x^2-1)(x+1)^{\delta}}\left(y^2\delta\left(x^3-x+1\right)+y^2\left(2-2\delta^3-x\right)\right)
\end{aligned}
$$

(2.7)

$$- \frac{(x-1)^\delta}{2\left(x^2-1\right)(x+1)^\delta} \left(x^2 \left(\delta + 3 - y^2 \delta \right) + x^3 \left(2\delta^2 - \delta - 1 \right) \right)$$

$$- \frac{(x-1)^\delta}{2\left(x^2-1\right)(x+1)^\delta} \left(-2\delta^2 x \left(\delta x + 1 \right) + y^2 x^2 \left(x^2 + x - 3 \right) \right)$$

2.2 Petrov Classification of the Zipoy-Voorhees Spacetime

The Petrov classification is a classification scheme of the trace-free part of the curvature tensor (Weyl tensor) based on their certain algebraic properties, developed by A. Z. Petrov [55, 65]. There are a couple of ways to obtain the Petrov classification of a spacetime. The most common is that which reduces the classification to an eigenvalue problem [55].

Due to the symmetries of the Weyl tensor, it can be written as the 6×6 matrix

$$\mathbf{C} = \begin{pmatrix} A & B \\ -B & A \end{pmatrix} \tag{2.8}$$

where A and B are traceless 3×3 matrices. The algorithm is to form a complex matrix

$$K = A + iB \tag{2.9}$$

and compute the three eigenvalues of the complex matrix K [55]. Relationships between the eigenvalues are used to classify the spacetime.

Another method exploits a null frame to construct invariants (Weyl scalars) from the Weyl tensor (a good reference is [64]). The Weyl scalars are constructed by contracting the Weyl tensor with various combinations of the null basis vectors. For the Zipoy-Voorhees spacetime, the Weyl scalars are computed in an upcoming

paper by Jeandrew Brink.

The main findings of this paper are that the parameter value $\delta = 0$ is flat space, namely the very special type-O spacetimes, with straight lines as geodesics. The parameter value $\delta = 1$ corresponds to the Schwarzschild metric, a type-D spacetime, which has integrable geodesics equations. For other spacetimes, the parameter δ then gives us an indication of how a spacetime deviates from physically understood spacetimes. The general case with $\delta \neq 1, 0$ corresponds to a type-I spacetime whose geodesic structure still has fully to be explored.

Chapter 3

Integrability of Dynamical (Hamiltonian) Systems

Geodesic equations of spacetimes can be written as Hamiltonian systems [56]. The integrability of such systems, specifically the equations of motion of the Zipoy-Voorhees spacetime is studied in this thesis.

A Hamiltonian system is integrable if it admits a full set of constants of motion (see definition 3.1.1). If a system is integrable we are able to completely solve it via quadrature. Otherwise, we say the system is "non-integrable". A noninte-grable system may be "nearly-integrable". This is a system for which there is a perturbation in the Hamiltonian of an integrable system given by

$$\hat{\mathcal{H}} = \mathcal{H} + \epsilon \mathcal{H}_1. \tag{3.1}$$

$\mathcal{H}$ is the unperturbed Hamiltonian which is a function of the "action-angles", $\mathcal{H}_1$ is the perturbation Hamiltonian and ϵ is sufficiently small, *i.e.* $\epsilon << 1$. In general this perturbation destroys integrability. For very small perturbations, canonical perturbation theory can be used to compute approximation to the solutions of the perturbed system of equations.

As an example of an integrable system which is perturbed, we consider a simple one dimensional case given by the equation

12

$$\frac{dX}{dt} = F(X) \tag{3.2}$$

We want to look at the steady state solution X_s which satisfies

$$F(X_s) = 0 \tag{3.3}$$

Suppose we introduce a perturbation ε so that

$$X = X_s + \varepsilon \tag{3.4}$$

where $\varepsilon << X_s$. Then differentiating gives

$$\frac{dX}{dt} = \frac{dX_s}{dt} + \frac{d\varepsilon}{dt} = \frac{d\varepsilon}{dt} = F(X) \tag{3.5}$$

We now Taylor expand $F(X)$ about the steady state solution X_s to give:

$$F(X) = F(X_s) + \left.\frac{dF(X)}{dt}\right|_{X=X_s} \varepsilon + \left.\frac{d^2F(X)}{dt^2}\right|_{X=X_s} \varepsilon^2 + ... \tag{3.6}$$

For sufficiently small ε, we can neglect the quadratic and all higher order terms. We then have

$$F(X) = F(X_s) + \left.\frac{dF(X)}{dt}\right|_{X=X_s} \varepsilon \tag{3.7}$$

But $F(X_s) = 0$, so equation (3.5) reduces to

$$\frac{d\varepsilon}{dt} = \left.\frac{dF(X)}{dt}\right|_{X=X_s} \varepsilon \tag{3.8}$$

Let $\left.dF(X)/dt\right|_{X=X_s} = \omega$. Then equation (3.10) can be written as

$$\frac{d\varepsilon}{dt} = \omega\varepsilon \tag{3.9}$$

whose solution is given by

$$\varepsilon = ce^{\omega t} \tag{3.10}$$

where $c = \varepsilon(0)$. With this we can analyze the perturbed system as a deviation from the steady state. If $\omega < 0$, $\varepsilon \to 0$ as $t \to \infty$ and the solution converges towards the steady state solution. We say that the solution is stable. On the other hand, if $\omega > 0$, $\varepsilon \to \infty$ as $t \to \infty$ and the solution diverges away from the steady state solution. In this case we say that the solution is unstable. In this chapter, I shall examine conditions for a system to be integrable. Also, I consider the stability of nearly integrable systems and relevant theorems that check "regions" of stability. Two of these are the "*Poincare-Birkhoff Theorem*" and the "*KAM theorem*". These theorems are useful when characterizing orbits exhibiting chaotic behavior.

3.1 Integrable Systems

I start by defining a spacetime and relevant properties. These are the objects on which we study the motion of timelike particles. It is worth mentioning since the tool we use to define the Hamilton's equation of motion, namely the Poisson bracket is rigorously defined as a map on the spacetime. The Hamilton's equations of motion is then discussed along with relevant theorem(s).

Spacetime is a smooth connected Lorentzian Manifold. Manifolds are topological spaces that is Hausdorff, locally Euclidean and has second countable bases [84]. Hamilton's equations of motion on a spacetime has an equivalent expression in terms of the Poisson bracket. In this section I start by introducing the concept of the Poisson bracket on a manifold and how it defines Hamilton's equations of motion. I then discuss definitions and theorems relating to the integrability of Hamiltonian systems.

The Poisson bracket is a bilinear map $\{ \bullet \}$, from a manifold to itself over the set of smooth functions on the manifold. The Poisson bracket is defined by

$$\{f, g\} = \sum_i \left(\frac{\partial f}{\partial q_i} \frac{\partial g}{\partial p_i} - \frac{\partial f}{\partial p_i} \frac{\partial g}{\partial q_i} \right) \tag{3.11}$$

where $f = f(p, q)$ and $g = g(p, q) \; \forall \; f, g \in C^\infty (\mathbf{M})$. Let the hamiltonian $\mathcal{H}$ be a smooth function on the manifold. We define the Poisson bracket of vector fields by $\{-, \mathcal{H}\}$ whose input arguments are again smooth functions. Hamilton's equations of motion we define as

$$\dot{q}_i = \frac{\partial \mathcal{H}}{\partial p_i} = \{q_i, \mathcal{H}\} \;\; , \;\; \dot{p}_i = -\frac{\partial \mathcal{H}}{\partial q_i} = \{p_i, \mathcal{H}\} \tag{3.12}$$

for smooth functions q_i and p_i, where the · indicates differentiation with respect to proper time τ. The q_i are the coordinates and the p_i are the conjugate momenta. The Hamilton's equations of motion are a system of equations whose solutions are integral curves (trajectories) associated with the vector fields in equation (3.12).

We now discuss a number of definitions and theorems pertaining to integrability in Hamiltonian systems.

Definition 3.1.1. *Let $\mathbf{M}$ be even dimensional, i.e. dim $(\mathbf{M}) = 2n$. A $2n$ system is said to be Louville integrable if it admits n Poisson commuting linearly independent functions (their gradients ∇p_i are linearly independent vectors on a tangent space at any point on $\mathbf{M}$), p_i, for $i = 1, ..., n$, so that $\{p_i, p_j\} = 0$ [94].*

A function which Poisson commutes with the Hamiltonian $\mathcal{H}$, *i.e.*$\{p_\mu, \mathcal{H}\} = 0$, is termed a conserved quantity or first integral and is very useful in simplifying our system of equations [94].

Poisson stressed that if p_i and q_i Poisson commute with $\mathcal{H}$ so does $\{q_i, p_i\}$. This is to say that if $\{q_i, \mathcal{H}\} = 0$ and $\{p_i, \mathcal{H}\} = 0$, then $\{\{q_i, p_i\}, \mathcal{H}\} = 0$. This gives the Jacobi identity on the poisson bracket. We cannot have more than n commuting quantities as this renders the Poisson bracket degenerate. The system in equation (3.12) is deterministic in that, given a set of initial conditions the behavior of the

system at a later time can be uniquely determined. The definition 3.1.1 will become useful when we study the equations of motion of the Zipoy-Voorhees spacetime in section 4.2 since the spacetime possesses two conserved quantities.

Let's introduce a coordinate transformation of phase space and explore the concept of "action-angles". We introduce the transformation.

$$Q_i = Q_i\left(p, q\right) \quad , \quad P_i = P_i\left(p, q\right). \tag{3.13}$$

If the transformation preserves the Poisson bracket, *i.e.*

$$\sum_{i=1}^{n} \left(\frac{\partial f}{\partial q_i} \frac{\partial g}{\partial p_i} - \frac{\partial f}{\partial p_i} \frac{\partial g}{\partial q_i} \right) = \sum_{i=1}^{n} \left(\frac{\partial f}{\partial Q_i} \frac{\partial g}{\partial P_i} - \frac{\partial f}{\partial P_i} \frac{\partial g}{\partial Q_i} \right) \tag{3.14}$$

$\forall\, f, g : \mathbf{M} \to \mathbf{R}$, then the transformation is called "canonical". These transformation equations also preserve the Hamilton's equations in equation (3.12).

Next we state the Arnold - Liouville theorem which helps us visualize trajectories from a geometrical viewpoint. Theorem 3.1.1 allows us to describe trajectories of the system as flows on the invariant tori foliated by the level surfaces. Theorem 3.1.1 will come in handy when we consider trajectories in the Zipoy-Voorhees spacetime in Chapter 4. The theorem is stated and discussed in [59].

Theorem 3.1.1. *Let $\left(\mathbf{M}, f_1, ..., f_n\right)$ be an integrable system with $\mathcal{H} = f_1$ and let*

$$\mathbf{M}_f := \{(p, q) \in \mathbf{M} : f_k\left(p, q\right) = c_k\} \quad , \quad c_k = constant\ for\ k=1,...,n$$

be an n-dimensional level surface of first integrals f_k. Then

• *If $\mathbf{M}_f$ is compact and connected then it is diffeomorphic to an n-dimensional torus*

$$T^n = S^1 \times S^1 \times ... \times S^1, \left(n - times\right)$$

and (in a neighborhood of this torus in $\mathbf{M}$) we can introduce the action-angle coordinates

$$P_1, ..., P_n, Q_1, ..., Q_n \quad , \quad 0 \leq Q_k \leq 2\pi$$

such that the angles Q_k are coordinates on $\boldsymbol{M}_f$ and actions $P_k = P_k(f_1, ..., f_n)$ are first integrals.

- *The canonical equations of motion become*

$$\dot{P}_k = 0 \quad , \quad \dot{Q}_k = \omega_k(P_1, ..., P_k) \qquad \text{for } k\text{=}1,...,n$$

and so the system is solvable by quadrature (a finite number of algebraic operations and integrations of known functions).

Suppose we have a function $S = S(q, P) : \mathbf{R}^{2n} \to \mathbf{R}$ with the condition that

$$det\left(\frac{\partial^2 S}{\partial q_j \partial P_i}\right) \neq 0 \tag{3.15}$$

We call S a "generating" function since it can be used to generate our action-angle coordinates. This is worth mentioning since it is the angle variables with which we associate the characteristic frequencies that are used to describe trajectories in the Zipoy-Voorhees spacetime in chapter 4. We then construct our transformation via the equations

$$p_i = \frac{\partial S}{\partial q_i} \quad , \quad Q_i = \frac{\partial S}{\partial P_i} \tag{3.16}$$

The transformation takes the canonical equations (3.12) to

$$\dot{P} = -\frac{\partial \mathcal{H}}{\partial Q} \quad , \quad \dot{Q} = \frac{\partial \mathcal{H}}{\partial P} \tag{3.17}$$

Consequently we obtain solutions to equation (3.17) in the form

$$P_i = c \quad , \quad Q_i = b + \tau \frac{\partial \mathcal{H}}{\partial P_i} \tag{3.18}$$

for arbitrary constants c, b.

Figure 3.1 shows the trajectory on the two dimensional torus. The action-angle variables are depicted on the right of the image.
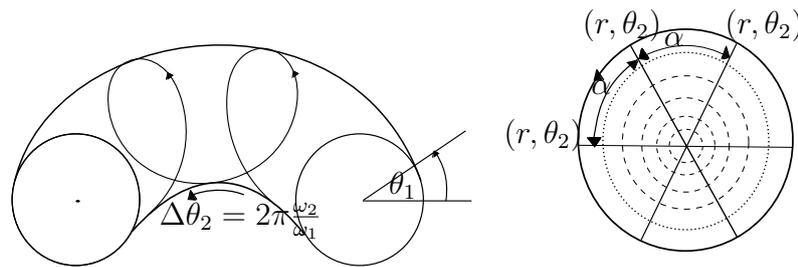
Figure 3.1. (a) shows orbit in an integrable system of two degrees of freedom. The orbit can be viewed as winding around a two dimensional torus with characteristic frequencies ω_1 and ω_2 associated with the angles θ_1 and θ_2 respectively. The ratio of the characteristic frequencies defines the shape of the orbit on the torus. A rational ratio defines a retracing of the trajectory. For an irrational ratio the trajectory densely fills the surface of the torus. (b) shows an advance of the angle θ for a surface of section of circular phase. The advance is constant in such case and is a function of the radius of the circle [30].

3.2 Non-Integrability and Chaos

At the beginning of this chapter I mentioned that perturbation in the Hamiltonian of the system in general destroys the integrability of the system. Another common signature of such system is the sensitive dependence on initial conditions. A small change in these initial conditions can have drastic effects on the state of the system at a later time. A system being nonintegrable means action-angle variables cannot be found (i.e. no generating functions can be found that can allow us to derive our action-angle variables).

Consider the evolution of a bundle of trajectories in phase space. If we are dealing with an integrable system, the bundle spreads linearly in time. However, were we to consider a non-integrable system the bundle evolution is non-linear. If we need to linearize the evolution we need a high level of accuracy in specifying the initial conditions. The inability to accurately specify initial conditions which would linearly evolve the bundles leads to the indeterminacy of the behaviour of the system over a long period of time. We then say our system's behaviour is chaotic. This was in opposition to the traditional view that if you give me a set

of initial conditions I will precisely predict the state of the system at a later time.

Most typical Hamiltonian systems exhibit behavior that lies somewhere between chaotic and non-integrable systems, these we call near-integrable systems.

3.3 Understanding Chaotic Hamiltonian Systems

At the turn of the twentieth century, the French Mathematician and Physicist Henri Poincaré took deep interest in understanding the stability of the solar system. This was in the days when nonlinear dynamics was in its infancy. It was and is seemingly trivial to most that orbits of planets around the sun in our solar system, for example, are stable. However, for physicists and mathematicians involved with research in celestial mechanics, the question of stability of such systems is crucial since they are interested in time scales that are large and need long term stability [66]. A time scale sufficiently large enough would allow for one to plausibly conclude that instability could arise. If the problem setup is sufficiently simple as in the "two-body problem" in Newtonian gravity it is completely integrable. The solution becomes cumbersome when a third body is considered. The typical example of the three-body problem is the sun and two planets. For $n > 3$ bodies it is called the many-body problem. Poincaré worked on this problem using canonical perturbation theory. The attempt was at viewing all other "bodies" as perturbations of a system of two bodies. Then an approximation to the solution of the system could be found. He however realized that there were series expansions with denominators that approached zero and did not converge. This is the well-known "problem of small divisors" that became a stumbling block in his quest for a solution to the many-body problem" [66]. He then suggested that such systems could not be solved analytically. Of course this was merely a conjecture since there did not exist computers then to numerically follow the orbits through longer time spans to conclude that instability could arise.

3.3.1   Poincaré Maps

The Poincaré map is very useful in studying the long term behaviour of chaotic orbits. It is a very powerful visualization tool that can be utilized to uncover details of the geometry of chaotic flows [63, 93]. This section gives some intuition of the construction of the Poincaré map and is a prelim to discussions on theorems that will play crucial roles in this thesis.

The onset of chaos in dynamical systems causes seemingly deterministic systems to show apparently random behavior. Understanding such "deterministic chaos" allows us to precisely understand the breakdown of determinism [93]. Consider the simplest case of a dynamical system which is governed by a system of first-order differential equations of the form

$$\frac{d}{dt}\mathbf{X}\left(t\right) = \mathbf{F}\left(\mathbf{X}\left(t\right)\right) \tag{3.19}$$

This system is continuous in phase space.

If instead of a continuous flow we discretize our system (representing the system as a map with discrete time). Then initial conditions would give the orbits as discrete points in time. The dynamical variables are iterated at the nth time to get their values at the $(n+1)^{th}$ time as in

$$\mathbf{X}_{n+1} = \mathbf{M}\left(\mathbf{X}_n\right) \tag{3.20}$$

See [93]. Usually an $n-1$ dimensional (for an n dimensional phase space) surface is chosen on which these points lie. The map is (in a sense) continuous since nearby points can be mapped to each other. These discrete points are points on the section through which the orbits pierce. A smooth flow thus determines a continuous map in $n-1$ dimensions which is invertible. A sufficiently large accumulation of these points form the Poincaré map. We note that the time elapsed between adjacent points will differ since the actual flow time elapsed between crossings will differ. The Poincaré map reduces a three dimensional flow to a two dimensional map which is easier to visualize.

Consequently, for a compact surface, we expect the flow to fold so that adjacent points remain separated as the flow continues [93].

3.3.2　Poincaré-Birkhoff Theorem

We saw in the subsection 3.3.1 that we can represent a flow in n dimensional phase space as an invertible map in $n-1$ dimensions. In the coordinate system of the action angle variables the surfaces of section will be concentric circles [63, 93]. Each point on these circles correspond to a pair of action angle variables. For convenience, we can use polar coordinates (*i.e.* (r, θ)) in place of the action-angles for its coordinate representation [67]. Then we can think of the orbit as winding around the torus. The winding orbit would represent an increase in θ ($\Delta\theta = \alpha > 0$). This is illustrated in figure 3.1. The ratio $\alpha/2\pi$ can be expressed as the ratio $\omega_2/\omega_1 = m/n$. We note that θ would vary as the radius changes. For different orbits (*i.e.* as we move between tori), the ratio will vary over both rational and irrational values.

We have different kinds of orbits. We have the simple periodic ones (where the point of piercing is mapped to itself), orbits with multiple periodicities (return to the start point over successive orbits), and those that have an irrational ratio of frequencies that and thus wind over the whole torus. For the first two cases these points are referred to as fixed points. These correspond to the rational values covered by the ratio $\alpha/2\pi$ called the "winding number".

Now, perturbing the Hamiltonian (*i.e* varying the action-angles) clearly affects the ratio $\alpha/2\pi$. Poincare was interested in the behavior of the orbits under such perturbation. He had a very good intuition that the stable orbits (those of fixed points) were likely to be disturbed under small perturbations in the Hamiltonian. Poincare conjectured in his 1912 paper [66] (and proved for special cases) that an area-preserving homeomorphic map from an annulus to itself admits at least two fixed points provided some twist condition is satisfied [12]. This twist, loosely speaking, involves rotating the two boundary circles in the opposite angular direc-
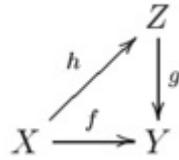
Figure 3.2. A lifting of f to Z.

tions. I now state the Poincare-Birkhoff Theorem more formally.

Firstly we give the definition of a "lifting". Consider an annulus given by

$$A = \{(a_1, a_2) \in R^2 : r_1^2 \le a_1^2 + a_2^2 \le r_2^2, 0 < r_1 < r_2\} \tag{3.21}$$

and denote the inner and outer boundaries of the annulus by C_1 and C_2 respectively. Consider a punctured plane (at the origin) and take a covering $H = R \times R_0^+$ of the punctured plane. Suppose we have a map

$$\chi : H \to R^2/\{(0,0)\} \tag{3.22}$$

given by

$$\chi(\theta, r) = r(cos\theta, sin\theta) \tag{3.23}$$

and we choose a subset $D \subset R^2/\{(0,0)\}$. Given a continuous map

$$\phi : D \to R^2/\{(0,0)\} \tag{3.24}$$

$\phi' : D' \to H$ is called a lifting of ϕ to H if

$$\chi \circ \phi' = \phi \circ \chi \tag{3.25}$$

where $D' = \chi^{-1}(D)$ [20].
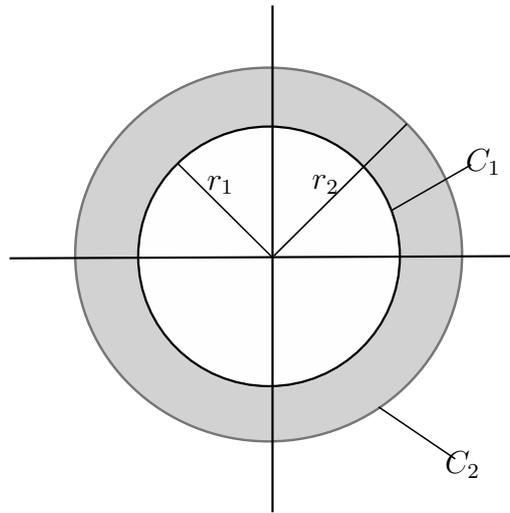
Figure 3.3. An annulus showing the boundary circles C_1 and C_2. Theorem 3.3.1 tells us that the restriction of the map ψ to the boundary sets C_1 and C_2 are the inclusion maps defined by $\psi(C_1) = C_1$ and $\psi(C_2) = C_2$ respectively.

Theorem 3.3.1. *(Poincaré-Birkhoff Theorem) [12, 20, 72] Let $\psi : A \to A$ be an area-preserving homeomorphism such that $\psi(C_1) = C_1$ and $\psi(C_2) = C_2$ where C_1 and C_2 are the boundary circles of A. Suppose there exists a lifting ψ' of ψ given by*

$$\psi'(\theta, r) = (\theta + g(\theta, r), f(\theta, r)) \tag{3.26}$$

where f and g are periodic in θ with period 2π. Then the homeomorphism ψ admits at least two fixed points in the interior of A provided

$$g(\theta, r_i) < 0 \tag{3.27}$$

for $i = 1, 2 \ \forall \ \theta \in R$. The condition in equation (3.27) is known as the twist condition [12, 20, 24, 72].

For the case of Hamiltonian systems this interprets as, under small perturbations in the Hamiltonian, the torus associated with the fixed points breaks down into

smaller tori. The breakdown of tori is more common with lower order rational ratio m/n.

There are two types of fixed points, namely $O-$fixed points and $X-$fixed points. The stable $O-$fixed points have oval-shaped neighborhoods known as the *Birkhoff Chains of Islands* [9, 77]. The width of the neighborhood increases as a system deviates from integrability [3]. The $X-$fixed points have neighborhoods of hyperbolic chaotic curves, with the curves forming thin layers around the Birkhoff Chains of Islands. For sufficiently small deviations the chaotic areas as seen on the surface of section are constrained to a small area. For an unperturbed curve equal number of the of the O and X fixed points will exist and be alternately arranged around the curve [93]. Figure 3.4 b.

3.3.3   KAM Theorem

The KAM Theorem investigates the stability of motion in Hamiltonian systems that are perturbations of integrable ones. We saw in the subsections 3.3.1 and 3.3.2 that Poincaré and Birkhoff investigated those orbits with rational winding numbers. However their investigation left unanswered the question of the stability of the other invariant curves. This question was answered by Kolmogorov, Arnold and Moser [5, 6, 67]. Precisely the question that the KAM theorem answered was what happens to the invariant tori as we increase the nonlinearity of the system? The answer was

"All invariant tori are preserved for sufficiently small perturbations."

KAM showed that for sufficiently irrational winding numbers all associated tori will remain stable under small enough perturbations [5, 6, 67]. These stable tori obey the irrationality condition

$$\left|\frac{\omega_1}{\omega_2} - \frac{m}{n}\right| > \frac{k(\epsilon)}{n^{2.5}} \tag{3.28}$$
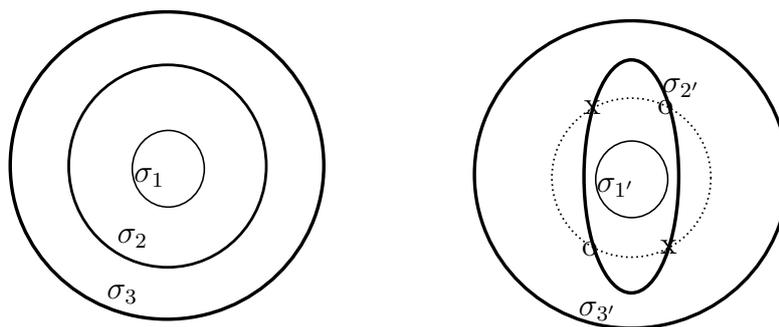
Figure 3.4. (a) shows an example of distortion of an invariant torus for $n = 2$ where the winding numbers σ_1 and σ_3 are irrational. σ_2 is rational with $n = 2$ resulting in 2 stable elliptical island (marked "O") and 2 unstable hyperbolic points (marked "X") under perturbation.

for some positive $\epsilon << 1$ [91] and n, m are integers.

The Arnold's irrationality criterion which is less restrictive is given

$$|\omega \cdot \mathbf{k}| > \frac{k\left(\epsilon\right)}{\mathbf{O}_{\mathbf{k}}^{n+1}} \qquad (3.29)$$

for vector of frequencies ω from the unperturbed hamiltonian, vector of integers $\mathbf{k}$ and n is the dimension of the vectors [91]. $\mathbf{O_k} = \sum_{i=1}^{n} |k_i|$ is the order of the resonance

Furthermore the KAM theorem gives us an indication of where chaos in a perturbed Hamiltonian may begin. It suggests that if chaos is to occur in such systems it will occur first at a torus associated with a rational ratio. These tori with rational ratios will firstly be destroyed. However, the KAM theorem does not tell us or guarantee when or whether they will be destroyed. Figure 3.4 shows the distortion and breakup of a resonant torus under perturbation [42]. It shows the stable elliptic O points and unstable hyperbolic X points.

For the stability of the solar system there is not a full answer to date [66]. However the KAM theorem can address the simpler case for three bodies. Consider, for example, the stability of the Earth's orbit under attraction from the Sun and say

Jupiter. The motion of each body would be represented by a torus embedded in 18 dimensional phase space (adjusted for the presence of conserved quantities). If we ignore the effect of the interaction between Earth and Jupiter we expect an irrational ratio of winding numbers (which would be equal to the Jupiter-Earth orbital period ratio). Thus we expect the Earth's orbit to be stable.

Finally, there is one thing we know from the KAM theorem. We can increase a perturbation by increasing the parameter that precedes the perturbing Hamiltonian. In effect, we are able to control the strength of the perturbation of a Hamiltonian system. A good example is the case of driven pendulum where we could increase perturbation by tuning up the driving amplitude. The idea of studying how the parameter affects the stability of the system is at the core of this thesis. In Chapter 4 we will see how the parameter of the Zipoy-Voorhees spacetime introduces chaos in the system. I shall investigate values of the parameter over which the system is nonintegrable.

3.3.4   Rotation Curves

Earlier in the subsection 3.3.2 we briefly stated what a winding number is. A more general term is the "*Rotation Number*". The map winding number, as stated in subsection 3.3.2, is the case where the rotation number takes on a rational value. It is the period of a quasiperiodic flow to pierce the same point in the surface of section [92]. For a circular surface of section of an integrable hamiltonian system the angle α is constant.

The rotation number is an invariant under homeomorphic maps of a circle (i.e. any space homeomorphic to a circle preserves the rotation number) [60, 66], so it can be calculated even for non-self intersecting continuous closed curves as in the case of surface of sections of nearly integrable systems. Then for such case we do not expect α to be constant. However, averaging α over all piercings (of a closed curve which corresponds to a specified set of initial conditions) still gives a good

indication of the characteristic frequency ratio of the system. More formally, let

$$T : R/Z \to R/Z \tag{3.30}$$

be homeomorphism of a circle. Consider the lifting

$$F : R \to R \tag{3.31}$$

Iterations of this lifting corresponds to evolution in time. Suppose we have an initial condition $\rho \in R$, then $F^n(\rho)$ is the system's state after the nth iteration. We define the rotation number in terms of the iterations of the lifting F as

$$\alpha(F) = \limsup_{n \to \infty} \frac{F^n(\rho)}{n} \, (mod \ 1) \tag{3.32}$$

If $\rho = (r, \theta)$ and with the assumption that F is one-to-one and continuous, $F^n(\rho) = (r_n, \theta_n)$ and the rotation number can be written as

$$\alpha(\rho) = \lim_{n \to \infty} \frac{\theta_n(\rho)}{n} \, (mod \ 1) \tag{3.33}$$

where ($(modulo \ 1)$ indicates 1 cycle which is equivalent to 2π) [63].

Physically we explain how this is calculated. Let us consider a closed curve in a Poincaré map corresponding to a specified set of initial conditions. Pick a piercing as a starting point and label it as i. The next piercing can then be labeled as $i + 1$. We label the angle between the ith and the $(i + 1)^{th}$ points relative to a fixed center of the Poincar'e map as θ_i. Similarly, θ_{i+1} gives the angle between the $(i + 1)^{th}$ and the $(i + 2)^{th}$ points relative to the same central point of the map and the process continues until the angle θ_n between the $(i + n)^{th}$ and the ith points is found. The average of these angles ($modulo \ 1$) gives the rotation number for the particular surface of section. For sufficiently large n, the limit

$$\alpha = \lim_{n \to \infty} \frac{1}{2\pi} \sum_{i=1}^{n} \frac{\theta_i}{n} \tag{3.34}$$

exists and gives the rotation number of the surface of section. Figure 3.5 shows
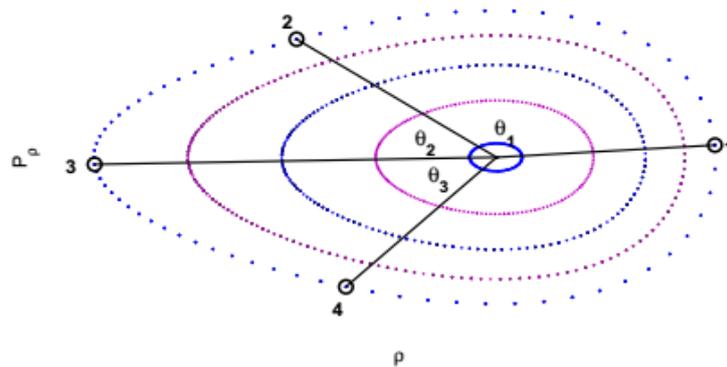
Figure 3.5. Given a particular Poincaré map the above figure shows how to compute the rotation number. The surfaces of section are plotted on the $\rho - p_\rho$ plane and each dot represents a piercing of this plane from below. The first "dot" is selected at (1) and a second successive dot at (2) is selected and the clockwise angle between them (relative to the centroid of the map) is computed. The angle between the dots at (2) and (3) is found and the iterative process is continued until the angle between the first and last point is computed. These angles are averaged and the rotation number is given by expressing the average as a fraction of a circle [30].

an example of a Poincaré map of a nearly integrable system and how the angular advance is used to determine the rotation number. For the spacetime considered in this thesis, there are two conserved quantities E and L_z due to the independence of the metric on t and ϕ (as we will see in Chapter 4). The characteristic frequencies associated with the remaining two coordinates are represented by ω_ρ and ω_z. The rationality of their ratio is related to the rotation number [30].

The rotation number can be expressed as a function of the radial coordinate ρ. The $2-D$ plot of the rotation number vs. ρ is known as the "rotation curve". For an integrable system such as the Kerr or Schwarzchild spacetime, the rotation curve is a smooth monotonically increasing (or decreasing) curve [30, 42]. When perturbation is introduced, there are breaks or plateaus on the curve at rational values of the rotation number and corresponding to resonant breaks in the small perturbation of regular motion. The plateau is indicative of the fact that within the neighborhood of the stable "O" points the rotation number remains constant. However, within the neighborhood of the unstable "X" points, the rotation number
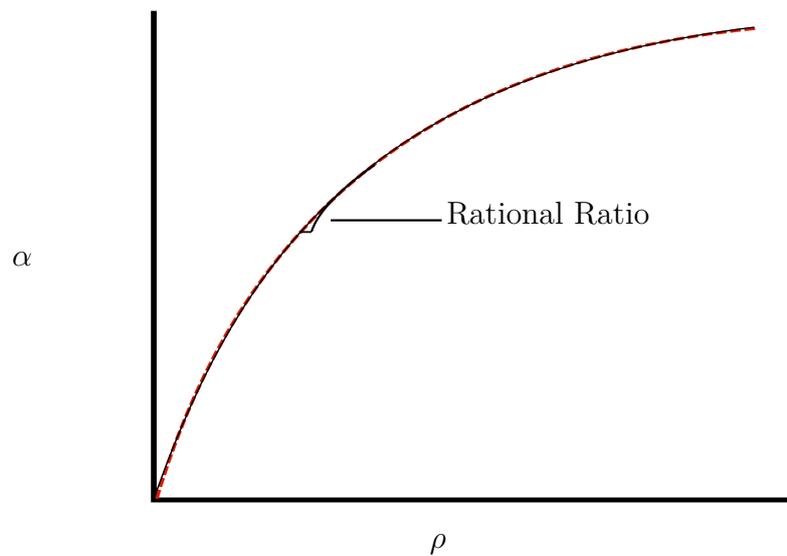
Figure 3.6. An example of a rotation curve. For a rational rotation number a plateau is present and indicates the constancy of the rotation number in the neighborhood of stable "O" points. The dash outlines the smooth curve that is indicative of the integrable system that was perturbed.

is not defined because of the chaos associated with the domain [6, 67, 70]. Figure 3.6 shows an example of the rotation curve of a perturbed system which is obtained by plotting the rotation number against the radial coordinate ρ. The plateau show that the rotation number remains constant in the neighborhood of the "O" points. The inflection point has undefined value for the rotation number since the region around the "X" point is chaotic.

In Chapter 4, the rotation curve will be used to study the integrability of the Zipoy-Voorhees spacetime.

Chapter 4

The Zipoy-Voorhees Spacetime

In this chapter, I study time-like trajectories in the Zipoy-Voorhees Spacetime. The presence of the parameter δ (defined in the metric of equation (2.1)) in the complex Ernst potential ϱ in equation (2.4) is a source of perturbation away from Schwarzschild (the case $\delta = 1$) and thus causes the breakdown of integrability of the equations of motion. Section 4.1 studies the effective potential (4.7) and (4.8). The effective potential is a useful tool (analogous to the Newtonian potential) in classifying orbits. The sign of the potential tells us where orbits can exist. This is done using plots of level surfaces of the effective potential in the $\rho - z$ plane.

In section 4.2 I investigate the integrability of the geodesic equations of the spacetime over certain values of the parameter δ. I make use of the Poincaré map to explore the breakdown of integrability. The Poincaré map is then used to construct the rotation curve in section 4.3 by computing the rotation number and plotting that against the starting ρ values for the orbits. The existence of island chains as discussed in section 3.3 would be indicative of chaos in the system. The size of this island also gives us a quantitative insight into of chaos in the system. For a comprehensive picture of the nature of these chains, several initial conditions are investigated. For each initial condition the orbit is integrated over very long time span and Poincaré maps produced.

4.1   The Effective Potential

The Zipoy-Voorhees metric and the components in local coordinates are given in section 2.1 equations (2.1),(2.2) and (2.3).

The inverse metric tensor is given by

$$g^{\mu\nu} = diag(-e^{-2\psi}, e^{2(\psi-\gamma)}, e^{2(\psi-\gamma)}, e^{2\psi}R^{-2}) \tag{4.1}$$

The Hamiltonian associated with the flow of the spacetime is given by

$$\mathcal{H} = \frac{1}{2}g^{\mu\nu}p_\mu p_\nu \tag{4.2}$$

where p_μ are the conjugate momenta obtained from the Langrangian of the metric by

$$p_\mu = \frac{\partial \mathcal{L}}{\partial \dot{q}_\mu}. \tag{4.3}$$

The spacetime's independence of t and its axial symmetry (independence of the metric on ϕ) would imply that $\dot{p}_t = \dot{p}_\phi = 0$ (from equation (3.12)). Thus we have two conserved quantities $p_t = -E$ and $p_\phi = L_z$. We also note that $g^{\mu\nu}$ is diagonal and that $g^{\rho\rho} = g^{zz}$. This gives the Hamiltonian as

$$\mathcal{H} = \frac{1}{2}[g^{\rho\rho}\left(p_\rho^2 + p_z^2\right) + g^{tt}E^2 + g^{\phi\phi}L_z^2] \tag{4.4}$$

We set

$$\mathcal{H} = -\frac{1}{2}\mu^2 \tag{4.5}$$

(where μ is the particle's rest mass) which is the Hamiltonian value along the particle's worldline.
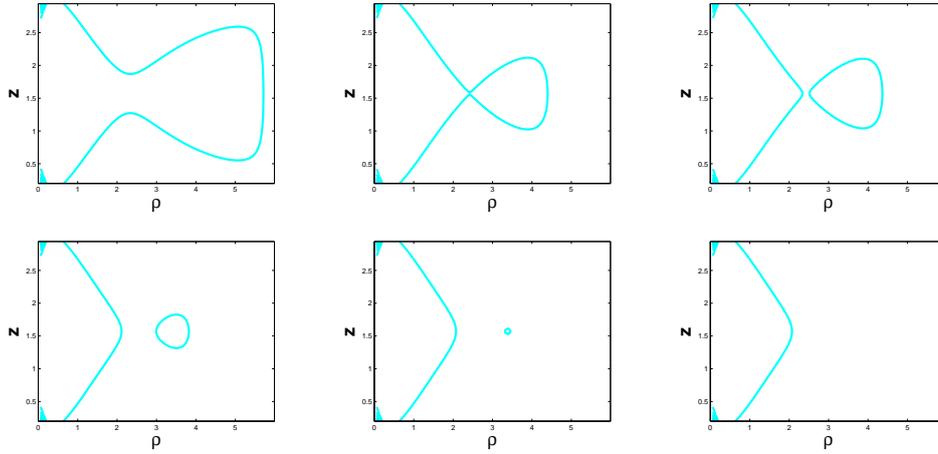
Figure 4.1. Plots showing the transition from nonbound orbits to bound orbits for $\delta = 1.65$ and $L_z = 6.25$. We see that for sufficiently high energy in the first plot there are no bound orbits. As the energy is lowered a neck (or throat) begins to form. At the critical energy of approximately $E = 0.97068$ the neck snaps and we have bound orbits. The region of the orbits continues to shrink as we further lower the energy until at approximately $E = 0.95625$ when the orbital region disappears.

Equating equations (4.5) and (4.4) we obtain

$$-\mu^2 = g^{\rho\rho}\left(p_\rho^2 + p_z^2\right) + g^{tt}E^2 + g^{\phi\phi}L_z^2 \tag{4.6}$$

Define

$$V = e^{-2(\psi - \gamma)}$$

and

$$G = -g^{\gamma\delta}p_\gamma p_\delta$$

where γ, δ runs over t and ϕ. Then equation (4.6) can be written as

$$J\left(\rho, z, E, L_z, \mu\right) = \left(G - \mu^2\right)V = \left(p_\rho^2 + p_z^2\right) \tag{4.7}$$

where J can be interpreted as the effective gravitational potential [11]. In terms

of local coordinates x and y we write the potential as

$$J = \left[\left(\frac{x+1}{x-1}\right)^{\delta} E^2 - \left(\mu^2 + \frac{(x-1)^{\delta-1}}{(x+1)^{\delta+1}(1-y^2)}L_z^2\right)\right]\frac{(x-1)^{\delta^2-\delta}(x+1)^{\delta^2+\delta}}{(x^2-y^2)^{\delta^2-1}}$$

(4.8)
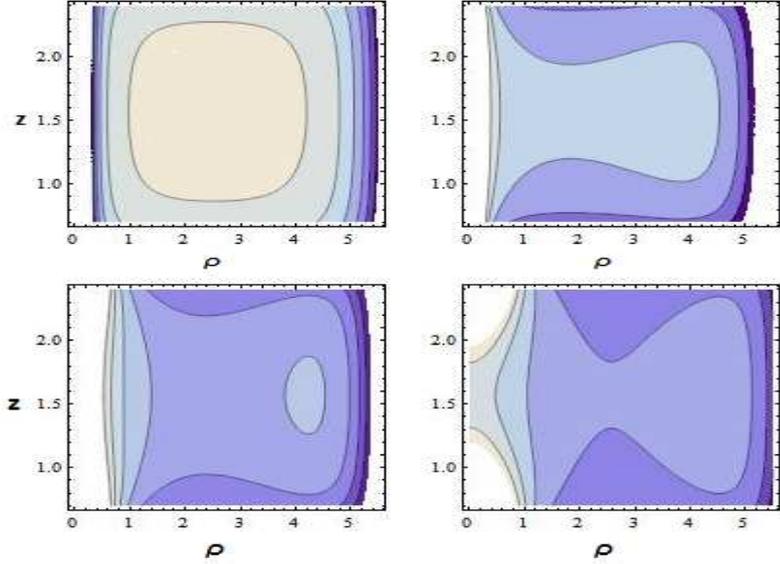
Figure 4.2. The Effective Potential plotted as level surfaces in the $\rho - z$ plane and symmetric about $z = \frac{\pi}{2}$, for $E = 0.98$ and $L_z = 7.5$. For the first plot in the first row $\delta = 0$ and the potential is negative. For the second plot in the first row $\delta = 1$ and the potential is positive for approximately $\rho < 0.5583$ but there is no closed orbit. For the first plot in the second row $\delta = 1.5$. The bounded region $3.80466 \leq \rho \leq 4.53321$ represents a bound orbit.

For massive particles that traverse timelike orbits, I set $\mu^2 = 1$ and equation (4.8) becomes

$$J = \left[\left(\frac{x+1}{x-1}\right)^{\delta} E^2 - \left(1 + \frac{(x-1)^{\delta-1}}{(x+1)^{\delta+1}(1-y^2)}L_z^2\right)\right]\frac{(x-1)^{\delta^2-\delta}(x+1)^{\delta^2+\delta}}{(x^2-y^2)^{\delta^2-1}}$$

(4.9)
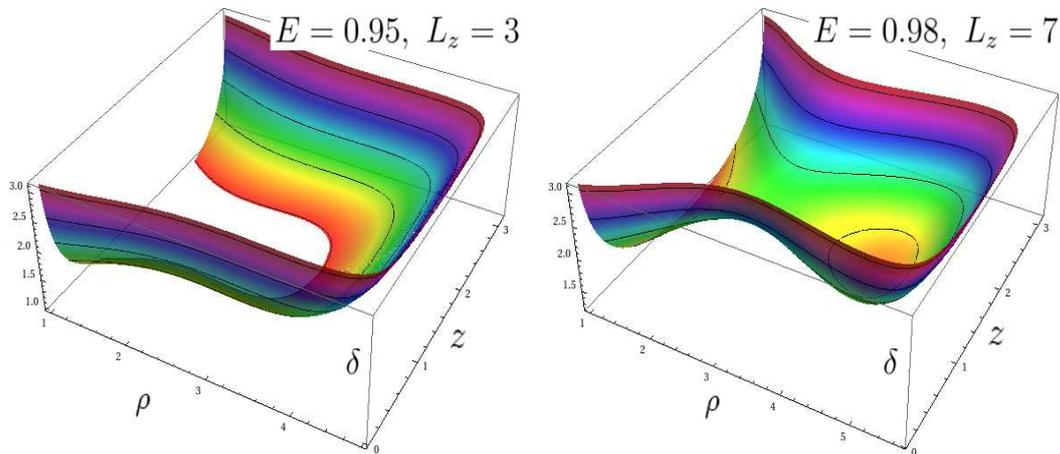
Figure 4.3. The first plot shows the potential for $E = 0.95$ and $L_z = 3$. It is evident that there are no bound orbits as delta is varied downwards (i. e. the level surfaces remain open at the bottom). The second plot shows the potential for $E = 0.98$ and $L_z = 7$. Bound orbits appear at approximately $\delta = 1.8048$. We see that the bottom of the level surfaces is closed. These pictures were taken from the talk "YES, YES, YES, to describing particle orbits in SAV spacetimes" given by Jeandrew Brink, Caltech, 2009.

A clearer way to see these regions is through physical space plots. These are plots of the effective potential as level surfaces in the $\rho - z$ plane and clearly show the regions of orbital motion (both bounded and unbounded). This is illustrated with the different plots in figure 4.2. Contours of the potential in the 3 dimensional ρ, z, δ space is also useful in that it gives us an immediate picture of the height of the potential with varying delta for fixed E and L_z as depicted in figure 4.3. Figure 4.1 shows level potential surfaces as well for fixed $L_z = 6.25$ and $\delta = 1.65$. At a sufficiently high energy, there is no bound orbit but we see the appearence of a neck at $\rho \approx 2.3603$. As the energy is reduced the neck shrinks. As the energy drops below $E \approx 0.97068$, the neck snaps and we have bound orbits. As the energy is further reduced the bound orbit shrinks until at about $E \approx 0.95625$ the circle disappears and we have no orbits.

The hypersurface $e^{2\psi} = 0$ sets the event horizon at $\rho = 0$. Incidentally the effective potential is divergent as $\rho \to 0$ for $\delta > 0$ which is an essential singularity. This says that in general the Zipoy-Voorhees spacetime contains a naked singularity
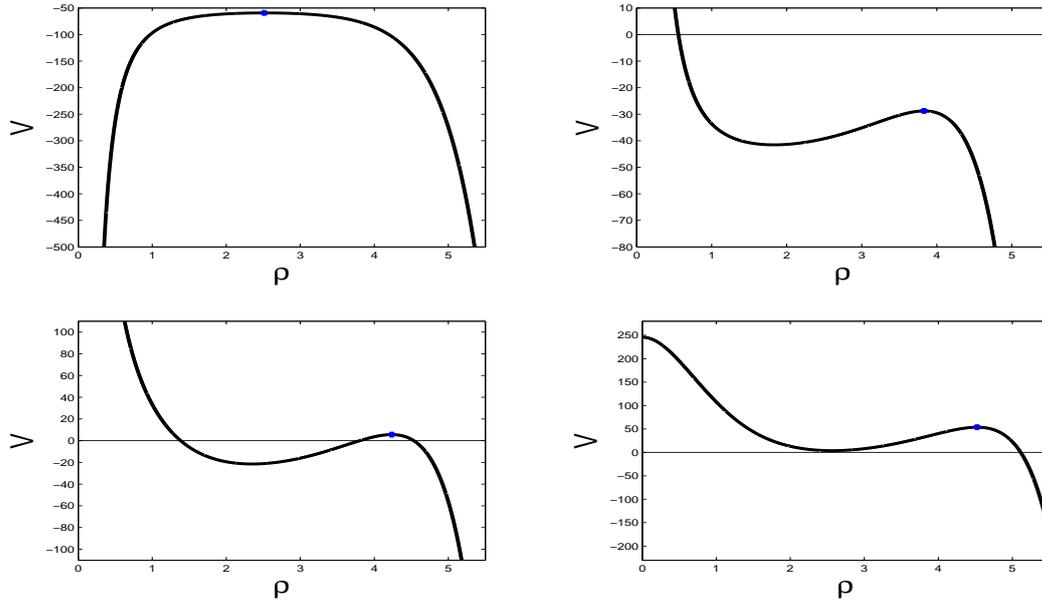
Figure 4.4. The effective potential plotted against ρ for $E = 0.98$ and $L_z = 7.5$ along the plane $z = \pi 2$. For the first plot in the first row $\delta = 0$ and the potential is everywhere negative. For the second plot in the first row $\delta = 1$. In this case an object crosses the potential barrier at approximately $\rho < 0.553$ but there is no bound orbit. For the first plot in the second row $\delta = 1.5$ with two bounded regions, $1.38429 \leq \rho \leq 3.80466$ and $3.80466 \leq \rho \leq 4.53321$. For the region $1.38429 \leq \rho \leq 4.53321$ the potential is negative. The bounded region $3.80466 \leq \rho \leq 4.53321$ represents a bound orbit. $\delta = 2$ in the second plot in the second row. Here the objects plunges in towards $\rho = 0$.

[47, 50, 62].

Equations (4.8) and (4.9) gives the effective potential for the Zipoy-Voorhees space-time. Along the equatorial plane, whenever the potential $J = 0$ we see that the constraint $J = p_\rho^2 + p_z^2$ would imply that $p_z = p_\rho = 0$. The name given to the curve formed by the roots of the potential along the selected plane is the CZV or curve of zero velocity. This curve is named so because $p_\rho = p_z = 0$ implies that $\dot{\rho} = \dot{z} = 0$ respectively. This means that when a geodesic reaches the CZV, there is a turning point (i.e the velocity components of the ρ and z coordinates are zero).

The CZV determines the set of initial conditions that permits geodesic motion.
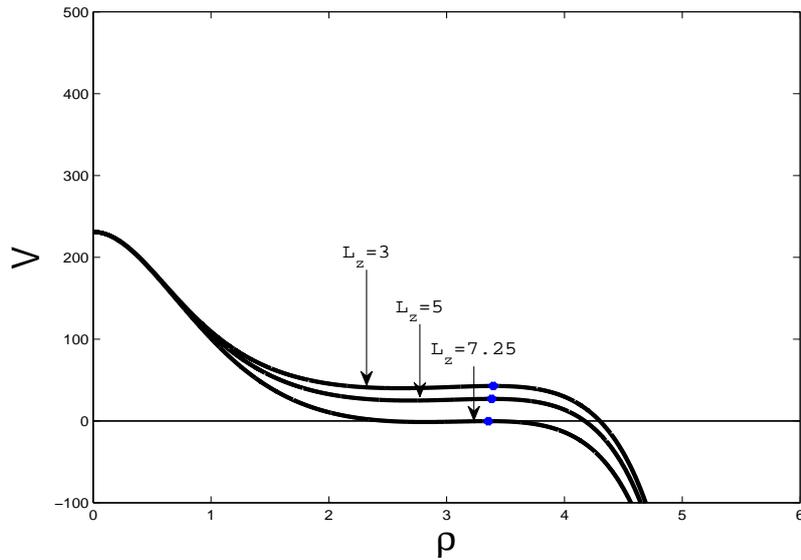
Figure 4.5. Plot of the effective potential J against the radial coordinates ρ with $\delta = 2$, and a fixed $E = 0.95$ along the plane $z = \pi 2$. For each curve on the plot, we see that as we increase L_z the maximum of the potential drops and shifts to the left. We see that if L_z is increased to about $L_z = 7.25$ the maximum of the potential drops below zero.

Consider the first plot in the bottom row of figure 4.4 with $\delta = 1.5$. We see that for $\rho < 1.38429$ we have a plunging orbit. The distinction between orbits that plunge and non plunging orbits is the result of the fact that there is a local maximum of the potential above zero.

Figure 4.5 shows several plots of the effective potential for $\delta = 2$ and a fixed $E = 0.95$ and varying L_z. The maximum of the potential for each curve on the plot is marked a blue $*$ and we see that as the momentum L_z increases that the local maximum is shifted towards the horizon and gets closer to the line $J = 0$. When L_z increases to about 7.25 the local maximum of the potential drops below zero and a saddle point appears. These saddle points correspond to unstable periodic orbits.

The unstable periodic orbits are called Lyapunov Orbits (LO) [17]. A geodesic around the central object will plunge as it crosses the LO. However, for certain
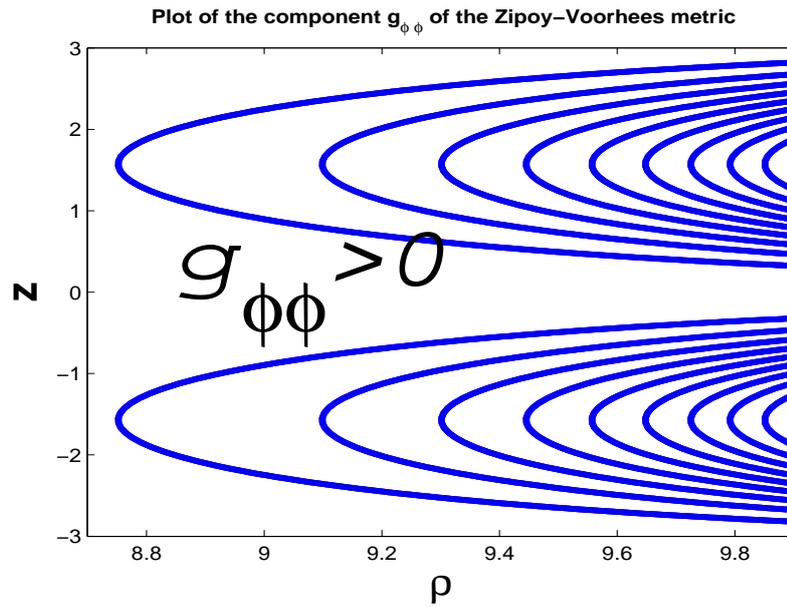
Figure 4.6. The plot of $g_{\phi\phi}$ as level surfaces in the $\rho - z$ plane for the Zipoy-Voorhees metric with $\delta = 2$. We see there are no closed time-like curves as $g_{\phi\phi}$ is strictly positive. This is true for all ρ, z and all δ.

values of energy and momentum we can locate a radial distance ρ such that $J = J' = J'' = 0$. This is to say that we solve the system

$$
\begin{aligned}
J &= 0 \\
J' &= 0 \\
J'' &= 0
\end{aligned}
\tag{4.10}
$$

for E, L_z and ρ. This becomes where the innermost stable circular orbit (ISCO) occurs. For orbits in the Zipoy-Voorhees spacetime about the equatorial plane the values are given by

$$\rho_{ISCO} = \cosh^{-1}\left(3\delta + \sqrt{5\delta^2 - 1}\right)$$

$$E_{ISCO} = \sqrt{e^{2\psi(\rho_{ISCO})}\frac{\cosh\left(\rho_{ISCO}\right) - \delta}{\cosh\left(\rho_{ISCO}\right) - 2\delta}} \tag{4.11}$$

$$L_{ISCO} = \sqrt{e^{-2\psi(\rho_{ISCO})}R^2\left(1 + E_{ISCO}^2 e^{-2\psi(\rho_{ISCO})}\right)}$$

For the Zipoy-Voorhees metric with $\delta = 2$, the $ISCO$ is located at $\rho_{ISCO} = 3.0286$. The first equation of equation (4.11) constrains δ and requires that $\delta \geq 1/\sqrt{5}$. For $\delta < 1/\sqrt{5}$ then the innermost stable circular orbit of the spacetime is not defined and from a dynamical viewpoint, the Zipoy-Voorhees spacetime can be a considered a perturbation of Minkowski spacetime rather than Schwarzschild.

Another property of the Zipoy-Voorhees metric is that it admits no closed time-like curves, i.e. $g_{\phi\phi} > 0 \ \forall \ \rho, z$. We see $g_{\phi\phi}$ as level surfaces in the $(\rho - z)$ plane in figure 4.6 for the case of $\delta = 2$.

Pictures of some orbits in the Zipoy-Voorhees spacetime are appended in appendix D.

Figure 4.4 shows the potential plotted against ρ. Here we have fixed $E = 0.98$ and $L_z = 7.5$. In the first plot we set the parameter $\delta = 0$. For $\delta = 0$ there is no bound orbits. Here the potential is everywhere negative. In the second plot from the top row, the potential starts becoming positive at approximately $\rho = 0.5583$. However, no closed orbit exists. The plot in the bottom left shows the potential for $\delta = 1.5$. There are two bounded regions in this case. One is the region $1.38429 \leq \rho \leq 3.80466$ and the other is $3.80466 \leq \rho \leq 4.53321$. However, for the region $1.38429 \leq \rho \leq 3.80466$ the potential is negative and we can have no orbits in such regions. An object in the second region oscillates between $\rho = 3.80466$ and $\rho = 4.53321$. This corresponds to a closed orbit. The plot in the bottom right shows the potential for $\delta = 2$. In this case the object plunges toward the singularity $\rho = 0$.

4.2   Orbits in the Zipoy-Voorhees Spacetime

In this section we study time-like geodesics in the Zipoy-Voorhees spacetime. The Schwarzschild's spacetime, which is a member of the family of the parametrized Zipoy-Voorhees spacetimes, is an integrable system. The geodesic equations of the Schwarzschild spacetime are integrable and analytic solution exists in terms of elliptic functions [76]. The Schwarzschild geodesics are discussed in appendix A.

The geodesic equations of a spacetime can be expressed using Hamilton's equations of motion as discussed in section 3.1. The δ in the Z-V metric destroys the integrability of the equations of motion. This makes obtaining of an analytic solution infeasible. I explore numerical solutions to understand how the parameter affect the integrability of the spacetime.

The Hamilton's equations of motion are given by the equation (3.12). For the Z-V metric these equations, in local coordinates are given by

$$\dot{p}_t = 0$$

$$\dot{p}_\rho = -\delta E^2 \frac{(x+1)^{\delta-1/2}}{(x-1)^{\delta+1/2}} - \delta \left(x^2 - y^2\right)^{\delta^2-1} \frac{(x-1)^{\delta-1/2}}{(x+1)^{\delta+1/2}} \left(p_\rho^2 + p_z^2\right)$$

$$+ x \frac{(x-1)^{\delta-2\delta^2}}{(x+1)^{\delta+2\delta^2}} \left(\frac{\delta \left(x^2-1\right)^{\delta^2-1/2} - \left(\delta^2-1\right)\left(x^2-1\right)^{\delta^2+1/2}\left(x^2-y^2\right)^{-1}}{\left(x^2-y^2\right)^{\delta^2-1}} \right) \left(p_\rho^2 + p_z^2\right)$$

$$- \frac{(x-1)^{\delta-3/2}}{2\left(x+1\right)^{\delta+3/2}} \left[\frac{(1-y^2)^{1/2}\left(x+2\delta\right) + y\left(x^2-1\right)^{1/2}}{\left(1-y^2\right)^{3/2}} \right]$$

$$\dot{p}_z = y \frac{\left(\delta^2-1\right)\left(1-y^2\right)^{1/2}\left(x^2-y^2\right)^{\delta^2-2}}{(x-1)^{\delta^2-\delta}\left(x+1\right)^{\delta^2+\delta}} \left(p_\rho^2 + p_z^2\right) - y \frac{(x-1)^{\delta-1}}{(x+1)^{\delta+1}\left(1-y^2\right)^{1/2}} \frac{L_z^2}{2}$$

$$\dot{p}_\phi = 0$$

$$(4.12)$$

and

$$\dot{t} = -\left(\frac{x+1}{x-1}\right)^{\delta} E$$

$$\dot{\rho} = \frac{(x-1)^{\delta-\delta^2}\,(x^2-y^2)^{\delta^2-1}}{(x+1)^{\delta+\delta^2}} p_\rho$$

$$\dot{z} = \frac{(x-1)^{\delta-\delta^2}\,(x^2-y^2)^{\delta^2-1}}{(x+1)^{\delta+\delta^2}} p_z \qquad (4.13)$$

$$\dot{\phi} = \frac{(x-1)^{\delta-1/2}}{(x+1)^{\delta+1/2}\,(1-y^2)^{1/2}} L_z$$

where x, y are defined in equation (2.2) and p_μ are defined in equation (4.3). The parameter δ is explored for values in the interval $\delta \in (0, 2)$. I numerically integrate the Hamilton's equations over these values and check for regions of instability.

A good way to look for these region of instability is to compute the Poincaré map for a given δ with specified '*energies*' and '*momenta*'.

Figure 4.8 shows a Poincaré map with $\delta = 2, E = 0.95, L_z = 3$. The plot is a subspace of the phase space and was plotted with initial conditions 2.7668 to 3.3168. Each surface of section is symmetric about the equatorial plane. The rotation curve for the Poincaré map in figure 4.8 is computed in the next section.

4.2.1 Matlab Implementation

In my thesis Matlab was employed throughout for numerical computations. The codes used to compute the Poincaré maps and subsequently the rotation curves were originally written by Jeandrew Brink and Marisa Geyer. The codes were then adapted to obtain the results I sought in this thesis.

The ODE45 integrator was used for the integration of the geodesic equations in (4.12) and (4.13). The tolerances of the integrator were set at 10^{-11} and 10^{-14} respectively for the relative tolerance and absolute tolerance. The time span was

set from 0 to 50000 with a time step of 0.01. However, the codes were run more that once for the obtaining of more points to improve accuracy of my computations. There is first a main function that I would simply refer here to as A that calls the integrator. The integrator takes in the function A_1, initial values, the time span, as well as the set tolerances. The initial values are vectors $[\rho\ z\ P_\rho\ P_z]$ where the initial ρ values are chosen by locating where the maximum of the potential occurs for specified E, L_z and δ. The initial z value is on the plane or $z = \frac{\pi}{2}$, and P_ρ and P_z both start at 0. I wrote a function to compute the maximum of the potential and its associated ρ value.

The function A_1 is a function called by A. This function calls two other functions which I will refer to as A_{11} and A_{12}. The function A_1 resolves the geodesic equations in equation (4.13). The function A_{11} resolves the potential once the energy E, the momentum L_z, the parameter δ and the y values (a matrix of ρ and z values) are specified. The function A_{12}, given the same input as A_{11}, reesolves the equations in (4.12).

The function A_1 is called in another function that I will refer to as B. This function also takes in E, L_z and δ. The function B picks out the z values from the output of A_1 and choose the one that is closest to the plane $z = \frac{\pi}{2}$ (the difference between the z value and the plane should be less that 0.01). The location of that z value in the output is noted.

To select the point to plot on the Poincaré map we check if the following conditions hold.

- The next point chosen should be located right after the first location.

- The difference between the z value of the output from A_1 at the first location and the plane should be less than 0.

- The difference between the z value of the output from A_1 at the next location (from the first item) and the plane should be greater than 0.
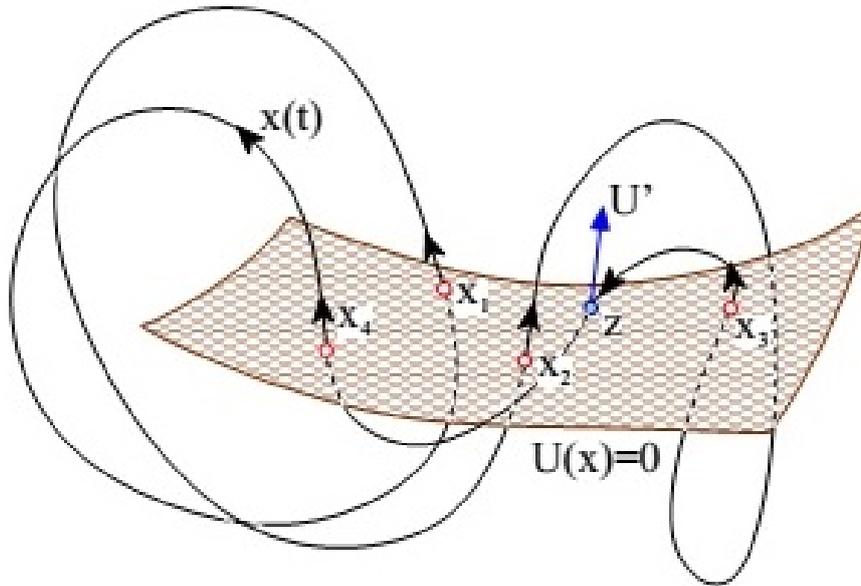
Figure 4.7. The figure shows the passing of orbits through a selected plane.

We then record the ρ values at those location. We also record the P_ρ values at those locations. A plot of the points in the (ρ, P_ρ) plane gives us the Poincaré maps. The functions A and B are then called in a function (which i refer to as C) that displays the output of the integration as well as plots of the orbits and Poincaré map.

The interpolation to compute the Poincaré map was necessary as we want to record points when the orbits pass through the plane. However, we are limited by the fact that the orbits themselves are discrete and collection of points. This means that we cannot necessarily record points on the surface. Instead, we try to choose points as close as possible to the plane.

Figure 4.7 shows the passing of orbits through a selected plane. The points x_1, x_2, x_3 and x_4 are the recorded points that appear on the Poincaré map.
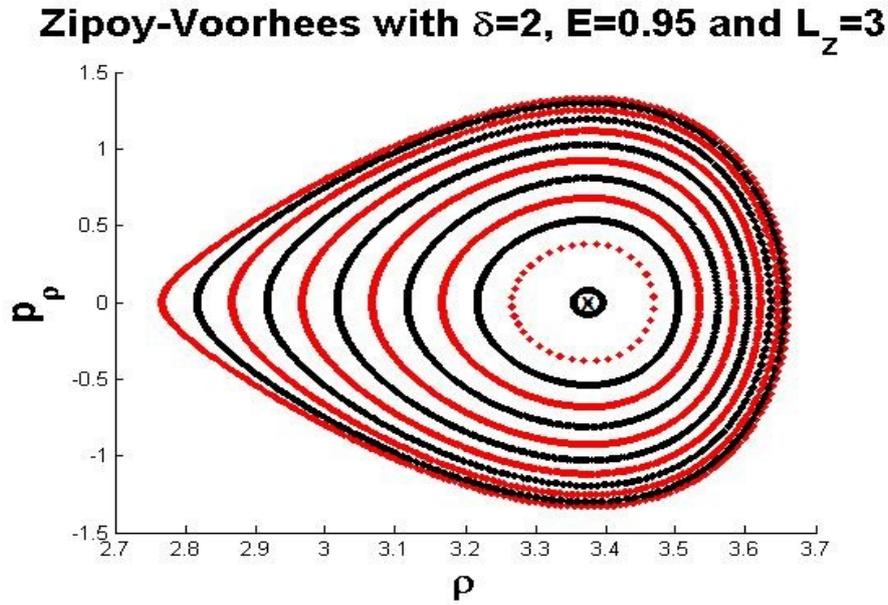
Figure 4.8. Poincaré map in the $\rho - p_\rho$ plane and symmetric about $p_\rho = 0$ with $\delta = 2$, $E = 0.95$ and $L_z = 3$.

4.3 The Rotation Curve of Orbits in the Zipoy-Voorhees Spacetime

In this section I compute the rotation curve and locate the 2/3 resonance. The rotation curve captures the location of resonant orbits. The appearance of a plateau at a resonance is useful for quantifying the size of these nonintegrable orbits.

The rotation number was discussed in section 3.3 and is defined in equation (3.34).The numerical evaluation involves the computation of angles between successive points on the Poincaré map and averaging these angles.

The rotation number is computed for each of the surface of section and then plotted against the minimum ρ values for the corresponding surface of section.
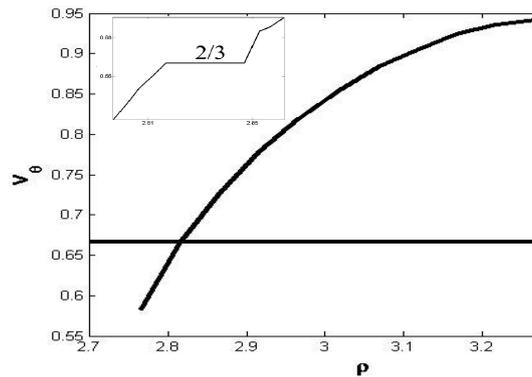
Figure 4.9. The Rotation curve for $\delta = 2$, $E = 0.95$ and $L_z = 3$. This rotation curve was computed from the Poincaré map shown in figure 4.8 by averaging the angles between successive points on each closed curve (each surface of section) per rotation. The 2/3 resonance occurs where the horizontal line crosses the curve.

4.3.1 Matlab Implementation

I first wrote a code that computes the centroid on the Poincaré map. The centroid (or center manifold) is computed by finding the smallest Poincaré section. The smaller the Poincaré section the more it approximates a circle. The code takes each section on the Poincaré map and finds the difference between the maximum and minimum ρ values. The section with the least difference is noted. For a very small Poincaré section the average ρ value of all the ρ values associated with that section approximates the ρ value of the centroid. This is plotted as $(\rho_{ave}, 0)$ on the Poincaré map in figure 4.8. It appears as a dot and it is marked by an X.

I then wrote a code that computes the rotation number by calling the function of the centroid and using the formula in equation (3.34). The function that computes the rotation number takes as input, the output from the integrator, E, L_z, δ, the output from the function that computes the centroid as well as the location of those recorded points on the Poincaré. The function for the rotation number is then called in the function C.

Figure 4.9 shows the rotation curve with the values $\delta = 2$, $E = 0.95$ and $L_z = 3$.

This rotation curve was computed from the Poincaré map in figure 4.8. We see that the 2/3 resonance occurs at $\rho = 2.8168$. The region on the rotation curve in figure 4.9 where the 2/3 resonance occurs is enlarged as shown in the inset. A plateau occurs at the 2/3 resonance. As we decrease the parameter $\delta = 2$ this resonant region shifts to the left. The size of the region also shrinks as will be discussed and visualized in the subsequent sections. This is expected as we see in figure 4.5, the ρ value at which the maximum of the potential occurs shifts to the left as we fix E and L_z and vary δ.

I call the size of the region the width. I will explore the width the system as it shrinks to zero and the system becomes more "integrable". The plots of these widths allows us to characterize the region of instability over different parameter values. This is the so called Arnold tongue and shall be discussed and computed in the next chapter for a simplified example to illustrate its properties analytically. Subsequently I compute it numerically for the Zipoy-Voorhees metric.

Chapter 5

Arnold Tongue of Instability

In this chapter I compute the Arnold tongue of dynamical instability for the Zipoy-Voorhees metric.

The rotation curve can be used to characterize the resonant region. The plateaus at these resonances gives a quantitative idea of the size of the nonintegrable region. For different parameter values the size of the plateau varies. Plotting these "widths" against their associated parameter values gives a plot referred to as the Arnold tongue. The Arnold tongue thus gives us a bound of the region of instability of a dynamical system.

As an example of the nonintegrability of dynamical systems, I start by exploring stability of systems modelled by the Mathieu's equation and computing the Arnold tongue analytically in section 5.3. This is a simple system that illustrates the nature of instabilities that occur in differential equations. As we shall see in section 5.3, for more complicated systems like that of the Zipoy-Voorhees metric, a numerical approach is currently needed.

5.1 The Mathieu's equation

An example of a parametrized equation that shows a tongue of instability is the Mathieu's equation given by

$$\frac{d^2x}{dt^2} + (\delta + \varepsilon \cos(t)) x = 0 \tag{5.1}$$

This equation can be derived from several physical scenarios. Try consider the situation sketched in figure 5.1 of two springs attached to a mass. If we explore the stability of the solution on the $y = 0$ plane ((5.4)), the Mathieu's equation naturally arises. The system is the differential equations that govern the spring

$$\frac{d^2x}{dt^2} + f_1(x,y)(x+1) + f_2(x,y)(x-1) = 0$$
$$\frac{d^2y}{dt^2} + f_1(x,y)y + f_2(x,y)y = 0 \tag{5.2}$$

where f_1, f_2 are given by

$$f_1 = k\left(1 - \frac{L}{\sqrt{(1+x)^2 + y^2}}\right)$$
$$f_2 = k\left(1 - \frac{L}{\sqrt{(1-x)^2 + y^2}}\right) \tag{5.3}$$

and $k = 1/2$ is the spring constant. The exact solution of equation (5.2) on the $y = 0$ plane is given by

$$x = A\cos(t)$$
$$y = 0 \tag{5.4}$$

for positive values of A. I test the stability of the system by introducing small
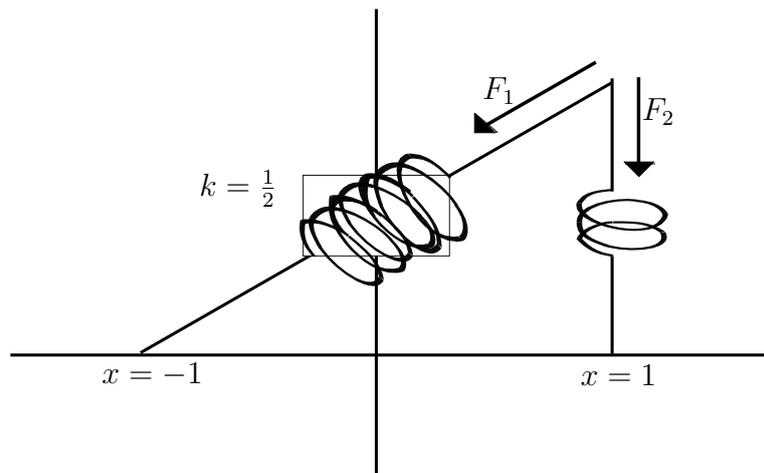
Figure 5.1. The above figure shows a spring of spring constant $k = \frac{1}{2}$ being stretched and compressed by forces F_1 and F_2 respectively.

deviations u, v from the solution in (5.4) to give

$$\begin{aligned} x &= A\cos\left(t\right) + u \\ y &= 0 + v \end{aligned} \tag{5.5}$$

I substitute the equations in (5.5) into the equations of motion in (5.2) and linearize in u, v. It is not difficult to verify that v obeys the Mathieu's equation (5.1) with

$$\begin{aligned} \delta &= \frac{2\left(1 - L\right) - A^2 L}{8} \\ \varepsilon &= -\frac{A^2 L}{8} \end{aligned} \tag{5.6}$$

5.2   Stability of Mathieu's Equation

I explore whether solutions for equation (5.1) with δ and ε given by (5.6) are bound (unstable) or unbound(unstable). Different methods exist for stability studies. These include the

1). Multi-time scale methods

2). Floquet theory

3). Harmonic balance

We study the stability of the system using the two time scale expansion.

I begin by introducing the two distinct timescales: One fast and the other slow:

$$
\begin{aligned}
\xi &= t \\
\eta &= \varepsilon t
\end{aligned}
\tag{5.7}
$$

and consider x to be expressed as $x(t) = x(\xi, \eta)$. So then we can write

$$
\frac{d^2 x}{dt^2} = \frac{\partial^2 x}{\partial \xi^2} + 2\varepsilon \frac{\partial^2 x}{\partial \xi \partial \eta} + \varepsilon^2 \frac{\partial^2 x}{\partial \eta^2}
\tag{5.8}
$$

Substituting equation (5.8) in equation (5.1) gives

$$
\frac{\partial^2 x}{\partial \xi^2} + 2\varepsilon \frac{\partial^2 x}{\partial \xi \partial \eta} + \varepsilon^2 \frac{\partial^2 x}{\partial \eta^2} + (\delta + \varepsilon \cos(\xi)) x = 0
\tag{5.9}
$$

Expanding x in powers of ε I obtain

$$
x(\xi, \eta) = x_0(\xi, \eta) + \varepsilon x_1(\xi, \eta) + \ldots
\tag{5.10}
$$

Substituting equation (5.10) into equation (5.9) and keeping term to order ε, we obtain the two equations

$$
\frac{\partial^2 x_0}{\partial \xi^2} + \delta x_0 = 0
\tag{5.11}
$$

$$
\tag{5.12}
$$

$$
\frac{\partial^2 x_1}{\partial \xi^2} + \delta x_1 = -\left(2 \frac{\partial^2 x_0}{\partial \xi \partial \eta} + x_0 \cos(\xi) \right)
\tag{5.13}
$$

The general solution to equation (5.11) is given by

$$x_0 = c_1 \cos\left(\sqrt{\delta}\xi\right) + c_2 \sin\left(\sqrt{\delta}\xi\right) \tag{5.14}$$

where c_i for $i = 1, 2$ are functions of η.

Differentiating equation (5.14) twice and substituting into the second equation of equation (5.11) gives

$$\frac{\partial^2 x_1}{\partial \xi^2} + \delta x_1 = 2\sqrt{\delta}\left(\frac{dc_1}{d\eta}\sin\left(\sqrt{\delta}\xi\right) - \frac{dc_2}{d\eta}\cos\left(\sqrt{\delta}\xi\right)\right)$$
$$- \cos\left(\xi\right)\left(c_1\cos\left(\sqrt{\delta}\xi\right) + c_2\sin\left(\sqrt{\delta}\xi\right)\right) \tag{5.15}$$

which can be written as

$$\frac{\partial^2 x_1}{\partial \xi^2} + \delta x_1 = 2\sqrt{\delta}\left(\frac{dc_1}{d\eta}\sin\left(\sqrt{\delta}\xi\right) - \frac{dc_2}{d\eta}\cos\left(\sqrt{\delta}\xi\right)\right)$$
$$- \frac{c_1}{2}\left(\cos\left[\left(\sqrt{\delta}+1\right)\xi\right] + \cos\left[\left(\sqrt{\delta}-1\right)\xi\right]\right) \tag{5.16}$$
$$- \frac{c_2}{2}\left(\sin\left[\left(\sqrt{\delta}+1\right)\xi\right] + \sin\left[\left(\sqrt{\delta}-1\right)\xi\right]\right)$$

<u>Finite solution:</u>

We remove the resonance terms by setting

$$\frac{dc_1}{d\eta} = \frac{dc_2}{d\eta} = 0 \tag{5.17}$$

(for a general δ).

However, suppose we choose $\delta = 1/4$. Then equation (5.16) becomes

$$
\begin{aligned}
\frac{\partial^2 x_1}{\partial \xi^2} + \frac{1}{4}x_1 &= \left(\frac{dc_1}{d\eta} \sin\left(\frac{\xi}{2}\right) - \frac{dc_2}{d\eta} \cos\left(\frac{\xi}{2}\right) \right) \\
&\quad - \frac{c_1}{2} \left(\cos\left(\frac{3}{2}\xi\right) + \cos\left(\frac{\xi}{2}\right) \right) \\
&\quad - \frac{c_2}{2} \left(\sin\left(\frac{3}{2}\xi\right) - \sin\left(\frac{\xi}{2}\right) \right) \\
&= \left(\frac{dc_1}{d\eta} + \frac{c_2}{2} \right) \sin\left(\frac{\xi}{2}\right) - \left(\frac{c_1}{2} + \frac{dc_2}{d\eta} \right) \cos\left(\frac{\xi}{2}\right) \\
&\quad - \left(\frac{c_1}{2} \cos\left(\frac{3}{2}\xi\right) + \frac{c_2}{2} \sin\left(\frac{3}{2}\xi\right) \right)
\end{aligned}
\tag{5.18}
$$

I again repeat the removal of resonance terms by setting

$$
\begin{aligned}
\frac{dc_2}{d\eta} &= -\frac{c_1}{2} \\
\frac{dc_1}{d\eta} &= -\frac{c_2}{2}
\end{aligned}
\tag{5.19}
$$

Differentiating the second equation of (5.19) with respect to η gives

$$
\frac{dc_2}{d\eta} = -2\frac{d^2 c_1}{d\eta^2}
\tag{5.20}
$$

Substituting the second equation of (5.19) in equation (5.20) gives

$$
\frac{d^2 c_1}{d\eta^2} - \frac{c_1}{4} = 0
\tag{5.21}
$$

The solution is exponential and so both c_1, c_2 grow exponentially. This would imply that at $\delta = 1/4$ the system is unstable.

Now let us expand about ε. This allows us to explore the behaviour of the system around the $\delta = 1/4$ neighborhood. We write

$$
\delta = \delta_0 + \varepsilon\delta_1 + \varepsilon^2\delta_2 + ...
\tag{5.22}
$$

where $\delta_0 = \frac{1}{4}$. Putting equation (5.22) in equation (5.1) and repeating the steps

through equations (5.7) to (5.11) we obtain the two equations

$$\frac{\partial^2 x_0}{\partial \xi^2} + \delta_0 x_0 = 0$$
$$\frac{\partial^2 x_1}{\partial \xi^2} + \delta_0 x_1 = -\left(2\frac{\partial^2 x_0}{\partial \xi \partial \eta} + x_0 \cos\left(\xi\right) + \delta_1 x_0\right) \tag{5.23}$$

Again repeating the steps to remove the resonance we obtain the following equations

$$\frac{dc_1}{d\eta} = \left(\delta_1 - \frac{1}{2}\right)c_2$$
$$\frac{dc_2}{d\eta} = -\left(\delta_1 + \frac{1}{2}\right)c_1 \tag{5.24}$$

This gives the equation

$$\frac{d^2 c_1}{d\eta^2} + \left(\delta_1^2 - \frac{1}{4}\right)c_1 = 0 \tag{5.25}$$

whose solution is given by

$$c_1 = a_1 \cos\left[\sqrt{\delta_1^2 - \frac{1}{4}}\eta\right] + a_2 \sin\left[\sqrt{\delta_1^2 - \frac{1}{4}}\eta\right] \tag{5.26}$$

and thus

$$c_2 = a_3 \cos\left[\sqrt{\delta_1^2 - \frac{1}{4}}\eta\right] - a_4 \sin\left[\sqrt{\delta_1^2 - \frac{1}{4}}\eta\right] \tag{5.27}$$

for some constants a_1, a_2, a_3, a_4. Therefore c_1, c_2 are bound (and thus stable) provided $\delta^2 - 1/4 > 0$. That is, provided $\delta_1 < -1/2$ or $\delta_1 > 1/2$. This would imply that the region of instability lies in the interval $\delta_1 \in \left(-\frac{1}{2}, \frac{1}{2}\right)$. Figure 5.2 shows the plot of the Arnold's tongue. This plots the parameter δ as a function of ε via the relation

$$\delta = \frac{1}{4} \pm \frac{\varepsilon}{2} \tag{5.28}$$

A more accurate computation of the Arnold's tongue can be done by considering more terms of the expansion. For example considering terms up to order two in
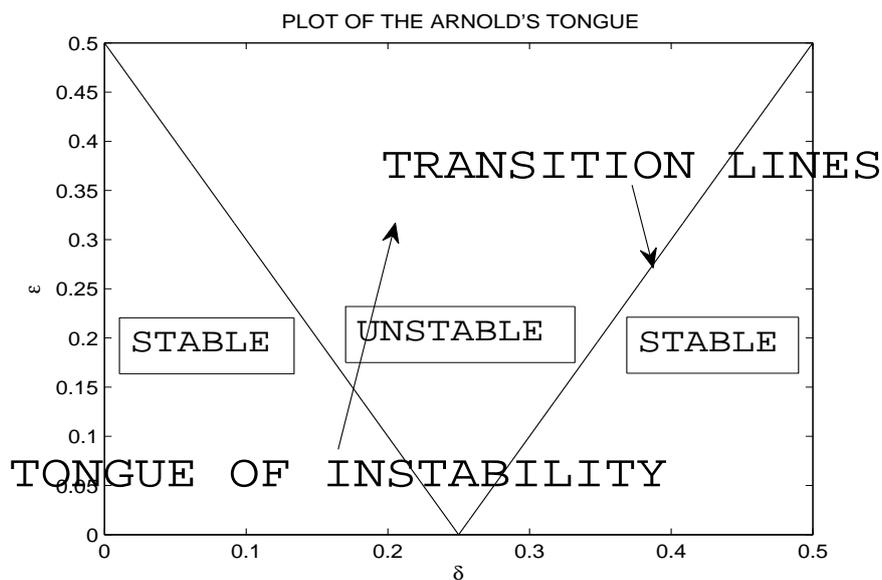
Figure 5.2. The above figure show the plot of the Arnold's tongue of the system in equation (5.1). We see that the transition lines ($\delta = 1/4 \pm \varepsilon/2$) separates the stable and unstable regions. The unstable region is the tongue of instability. This linearity in the transition lines is due to the truncation of the series expansion of δ in ε at the first order.

the expansion would produce quadratic terms of ε. In the next section I study the stability of resonant orbits in the Zipoy-Voorhees spacetime by computing the Arnold tongue. This time the computation is done numerically due to the presence of the non-linear parameter δ in the spacetime.

5.3 The Arnold's tongue in the Zipoy-Voorhees Spacetime

In section 4.3 I computed the rotation curve and located the 2/3 resonance at $\rho = 2.817$. I then enlarged the region around the 2/3 resonance as shown in the embedded diagram in figure 4.9 to see how wide the plateau occurring at the resonance was. The idea is to compare the size of this chaotic region with the

phase space. Decreasing the value of the parameter δ from $\delta = 2$ reduces the size of the chaotic region and the system becomes more stable as can be seen in the plots in figure 5.3.
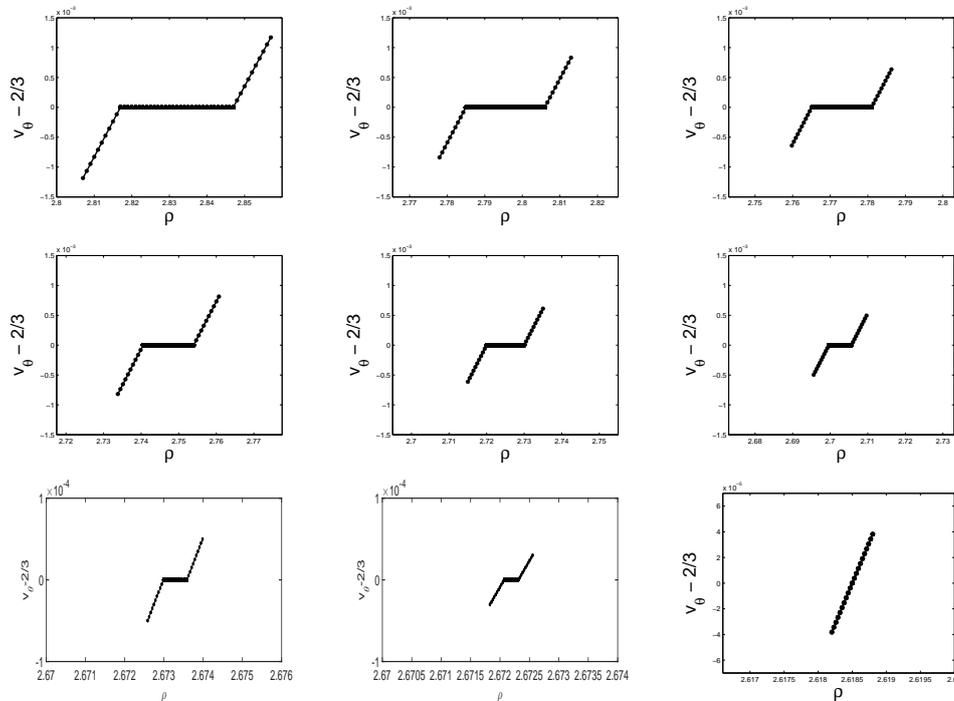
Figure 5.3. The figure shows the plots of the resonant regions for different δ values in the interval $\delta = 2 : -0.05 : 1.6$ from top to bottom. We see the shrinking width until at $\delta = 1.6$ when the width is zero.

The plots in figure 5.3 show the resonant regions for $\delta \in [1.6, 2]$. Increments of 0.05 were considered. I subtract 2/3 from the vertical axis to shift the 2/3 resonance to the zero horizontal line. It is found that the resonant plateaus vanish at $\delta = 1.6$. The relationship between the plateau width (w) and the parameter (δ) characterizing the perturbation strength is shown in the plot in figure 5.4. This plot indicates that the width of the plateau is quadratic in ρ. Table 5.1 gives the dependence of the width of the plateau and the average ρ value along the plateau as a function of δ. The average ρ value is useful indicator of the linearity of change in width of the plateau and δ changes. This gives us an idea of how fast the tongue
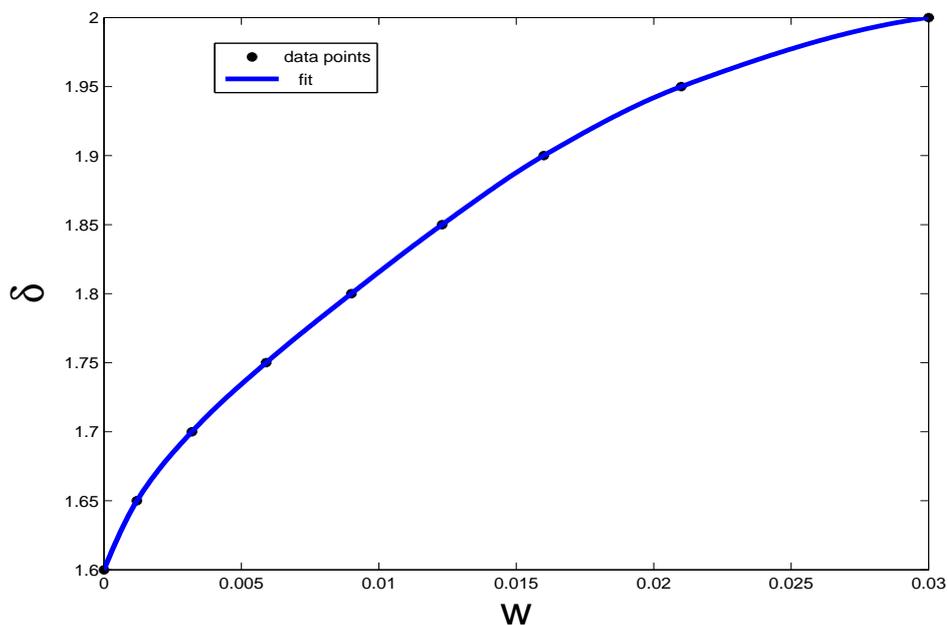
Figure 5.4. The figure shows δ plotted against the widths.

closes. We see the width decreases for smaller values of δ. The same is true for the average ρ value. Figure 5.5 plots the values in table 5.1 of the average ρ values against δ.

The fact that the plateau vanishes well before the Schwarzschild limit is reached is akin to the delay of the onset of chaos seen in damped systems. This is a very interesting phenomenon since it may suggest that, when the system is perturbed away from Schwarzschild, the system remains integrable for longer than expected. This case in which integrability is maintained is good for determining multipole moments of the spacetime from observations as canonical perturbation theory captures the distortions. A very fine grained search still has to be carried out to determine whether other forms of instability exist below $\delta = 1.6$. For example, instability may appear as we move away from Schwarzschild and the tongue could grow to a maximum width and start to close up until the system becomes integrable again at $\delta = 1.6$. This is a strange albeit unlikely possibility and could
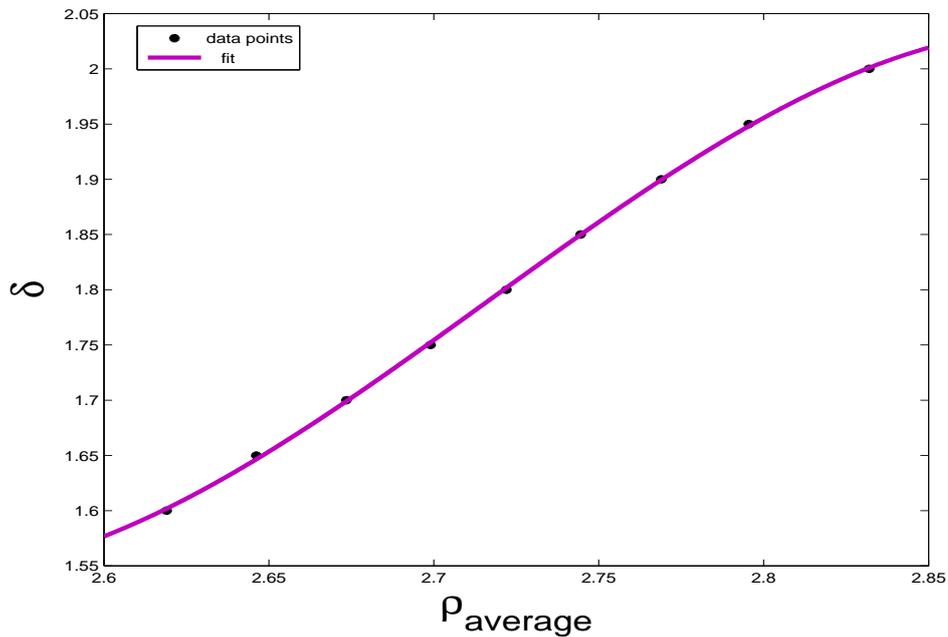
Figure 5.5. The figure shows plotted against the average ρ values.

possibly be a future research topic. Figure 5.6 shows the two possible cases.

Figure 5.7 shows all the blown up regions for the various δ in table 5.1 on one plot. We plot $(v_\theta - 2/3)$ against $(\rho - \rho^*)$ where ρ^* is where the first differential of the potential $\mathcal{V}'$ vanishes (i.e. where the potential is maximum). The term $(\rho - \rho^*)$ gives the distance of the chaotic region from the maximum of the potential. At the 2/3 resonance the plot is then an indication of how far the chaotic region is from the maximum of the potential in each case as we change δ. Clearly in figure 5.7, as δ is decreased, the width reduces but at this point the chaotic region is further away from the maximum.

Figure 5.8 shows the Arnold tongue with δ plotted as a function of ρ. The width is zero at $\delta = 1.6$ which is far removed from the Schwarzschild case $\delta = 1$. This indicates that the spacetime should appear "integrable" at $\delta = 1.6$. Comparing the Arnold tongue of the Zipoy-Voorhees spacetime (for the 2/3 resonance) shown in

Table of δ vs. widths of plateau w and the average ρ values $\rho_{average}$		
δ	w	$\rho_{average}$
2.00	0.03000	2.83200
1.95	0.02100	2.79550
1.90	0.01600	2.77300
1.85	0.01230	2.74715
1.80	0.00900	2.72450
1.75	0.00590	2.70295
1.70	0.00285	2.67217
1.65	0.00072	2.67196
1.60	0.00000	2.61850

Table 5.1. The table above shows δ against the width of the associated chaotic region as well as the average ρ value along the region. The width decreases as δ gets smaller. The average ρ value also decrease as δ gets smaller.

figure 5.8 to that of the Mathieu's equation shown in figure 5.2 we can make some statement(s): as ρ is a function of δ (and vice versa), it is clear from figure 5.8 that this relationship is nonlinear. In fact, rather than ρ being some polynomial function of δ (of degree > 1), this relationship seems much more complicated and will pose serious computational difficulties were one to attempt and analytic solution for the Arnold tongue.

5.3.1   Some Astrophysical Implications

The computation of the Arnold tongue has some astrophysical implications as well. For the case of $\delta = 2$, we see that the perturbation (quantified by the corresponding width in table 5.1), is very pronounced. The resonance associated with the value $\delta = 2$ is located at approximately $\rho = 2.817$. From equation (C.1) in appendix C, and noting the relationship between x and ρ from equation (2.2) in chapter 2, $\rho = 2.817$ corresponds to 9.393 in terms on r which is $4.69r_s$. For the parameter value $\delta = 1.6$, the 2/3 resonance occurs at approximately $\rho = 2.618$. this corresponds to $4r_s$. This is interesting as this means that the entire region of numerical chaos lying within the Arnold tongue of figure 5.8 is located between
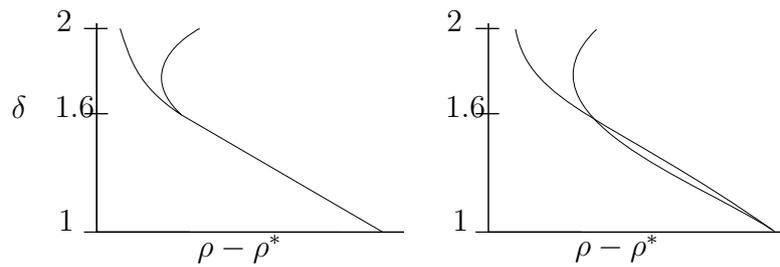
Figure 5.6. The first figure shows the system remains integrable up to $\delta = 1.6$ when the tongue starts opening up. The second figure shows the opening up of the tongue above $\delta = 1$ and closing at $\delta = 1.6$ and then opening up again above $\delta = 1.6$.

$4r_s$ and $4.7r_s$. For compact objects inspirals into supermassive blackholes, this is well within the sensitivity band of space-based detectors [42].

Another interesting aspect worth mentioning is this: for the Zipoy-Voorhees spacetime $\delta = M$ [87, 98] (where M is the mass of the blackhole). This would mean that smaller regions of numerical chaos (located closer to the horizon r_s) which is associated with smaller values of δ corresponds to smaller M. This in fact does make sense since $\delta = 0$ means $M = 0$ and the spacetime reduces to Minkowski spacetime.
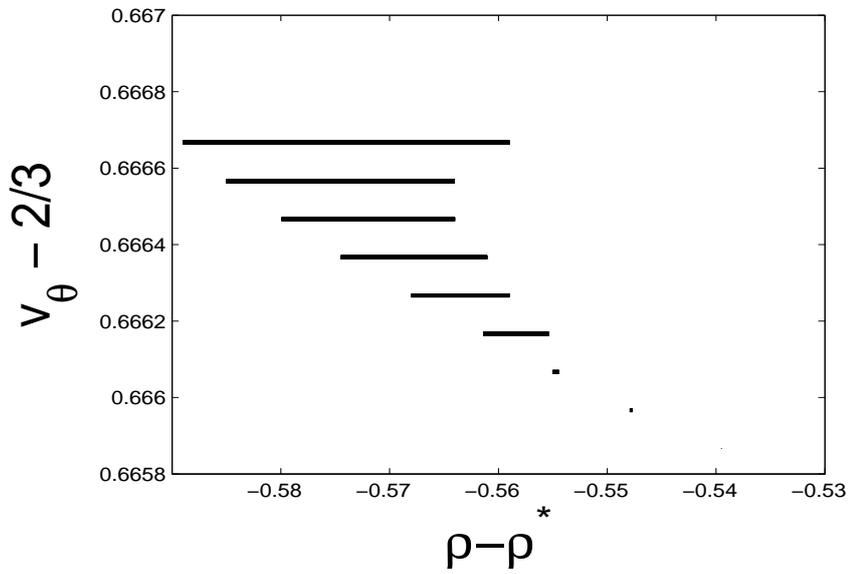
Figure 5.7. The above figure shows the blown up regions of the 2/3 resonance on one plot. The ρ axis is translated to the left by the maximum of the potential ρ^*. Each successive region is shifted down the y axis by 0.0001.
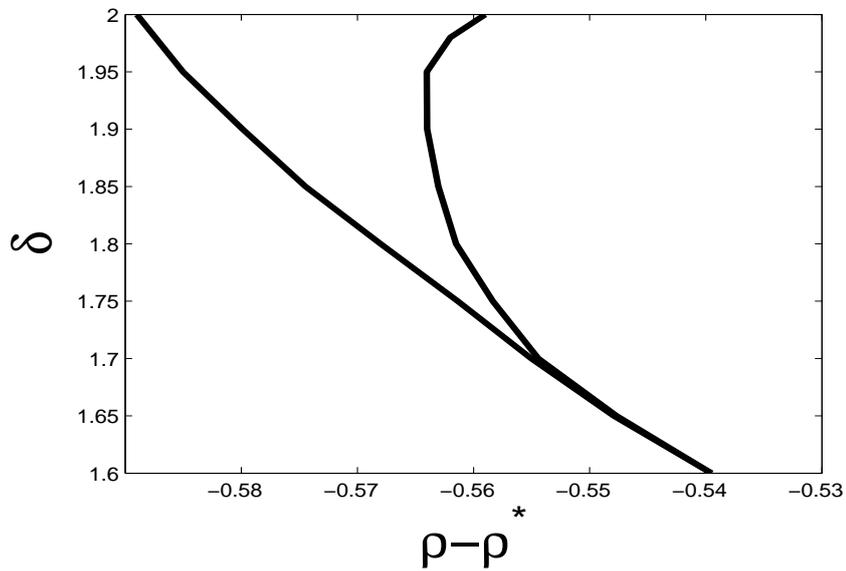
Figure 5.8. The figure shows the Arnold tongue for the 2/3 resonance in the Zipoy-Voorhees Spacetime for $E = 0.95$ and $L_z = 3$.

Chapter 6

Conclusion and Suggestions on Future Research

In this thesis I studied the integrability of the Zipoy-Voorhees spacetime using the Poincaré map and the rotation number as indicators of the breakdown of integrability. Using the rotation curve I computed the Arnold tongue. First it was seen that for the parameter value $\delta = 2$ of the Zipoy-Voorhees spacetime, a chaotic region appears as a plateau in the rotation curve at the 2/3 resonance at the approximate radial value of $\rho = 2.817$. The Zipoy-Voorhees spacetime is, for general δ, nonintegrable due to the presence of the regions of numerical chaos. However, as pointed out in [54], when the chaotic region is very small compared to the phase space covered by tori on which the orbits can move, the behavior is very similar to an integrable system. We have shown this to be the case with the Zipoy-Voorhees spacetime.

For $\delta = 1$ (the Schwarzschild's case) the Zipoy-Voorhees spacetime is integrable. We would expect that increasing the perturbation parameter would lead to the system becoming increasingly chaotic. However, numerically we saw that the onset of chaos is delayed for large parameter departures from Schwarzschild. For the particular resonance investigated (the 2/3 resonance), chaos started to appear at the value of $\delta = 1.6$ away from $\delta = 1$. The delay of the onset of chaos in a

system is usually associated with a damped oscillator. However, we are looking at a Hamiltonian system and these are undamped systems, so this behaviour is unusual and unexpected.

Possible future research include an attempt at analytically finding the width of the region of chaos for the 2/3 resonance. This would allow us to precisely locate the δ value at the onset of chaos.

There are also physical implications. The Zipoy-Voorhees in general is considered a perturbation of the Schwarzschild spacetime. The rotation number which is a very useful indicator of the size of the non-integrable region, is the ratio of the radial and azimuthal frequencies of a nonplunging orbit. Failure of integrability that may be observed in the gravitational wave signal can be quantified using the rotation curve. Such studies have been done for the Kerr metric. For example in [28], Lukes-Gerakopoulos, Apostolatos and Contopoulos studied the orbits of the Manko-Novikov metric (a perturbation of the Kerr metric) extensively. They also found that large deviation from Kerr occur in the closed inner CZV. In 2013, Marisa Geyer [30] did a full characterization of where resonances were likely to occur for all orbits in the Manko-Novikov metric.

The departures of integrabilty, as the Hamiltonian is perturbed away from that which describes the Schwarzschild metric, as quantified in this thesis, provide an important stepping stone in quantifying the effect non-self-force perturbations will have on gravitational wave signals.

Appendix A

Time-like Orbits in the Schwarzschild Spacetime

The Schwarzschild metric is given by

$$ds^2 = -\left(1 - \frac{r_s}{r}\right) dt^2 + \left(1 - \frac{r_s}{r}\right)^{-1} dr^2 + r^2 \left(d\theta^2 + sin^2\theta d\phi^2\right) \qquad \text{(A.1)}$$

The Lagrangian, in terms of the arclength s is given by

$$\mathcal{L} = -\left(1 - \frac{r_s}{r}\right) \dot{t}^2 + \left(1 - \frac{r_s}{r}\right)^{-1} \dot{r}^2 + r^2 \left(\dot{\theta}^2 + sin^2\theta\dot{\phi}^2\right) \qquad \text{(A.2)}$$

where the dot overhead indicates differentiation with respect to arclength. In terms of the proper time τ, the Lagrangian can be written as

$$\ell = \left(1 - \frac{r_s}{r}\right) \dot{t}^2 - \left(1 - \frac{r_s}{r}\right)^{-1} \dot{r}^2 - r^2 \left(\dot{\theta}^2 - sin^2\theta\dot{\phi}^2\right) \qquad \text{(A.3)}$$

which follows from the definition $ds^2 = -d\tau^2$. In this case, the . overhead indicates differentiation with respect to proper time.

The independence of the metric on t and ϕ provides us with constants of motion

along the t and ϕ directions as in the equations

$$\left(1 - \frac{r_s}{r}\right)\dot{t} = E$$
$$-r^2 sin^2\theta\dot{t} = L \tag{A.4}$$

respectively, where E represents the energy per unit mass and L represents the angular momentum per unit mass. We consider the case of motion along the equator, i.e. $\theta = \frac{\pi}{2}$.

By substitutions and rearrangements, the Lagrangian becomes

$$\ell = \left(1 - \frac{r_s}{r}\right)^{-1} E^2 - \left(1 - \frac{r_s}{r}\right)^{-1}\dot{r}^2 - \frac{L^2}{r^2} \tag{A.5}$$

For time-like geodesics, $\ell=1$, and writing the above equation in terms of the radial change with respect to proper time we have

$$\left(\frac{dr}{d\tau}\right)^2 = E^2 - \left(1 - \frac{r_s}{r}\right)\left(\frac{L^2}{r^2} + 1\right) \tag{A.6}$$

where we recognize the second term as the effective potential V_{eff}. Figure A.1 shows the plot of the potential of the Schwarzschild metric for different $L's$. We should note that the lowering of the peak of the potential as L decreases is in agreement with how I defined my constants of motion (i.e. the energy per unit mass E is positive and the momentum per unit mass L is negative).

The above equation can be integrated to write r in terms of the proper time τ. But we are interested in the shape of the geodesic, i.e. r in terms of ϕ. By the chain rule,

$$\frac{dr}{d\tau} = \frac{dr}{d\phi}\frac{d\phi}{d\tau} \implies \left(\frac{dr}{d\tau}\right)^2 = \left(\frac{dr}{d\phi}\right)^2\left(\frac{d\phi}{d\tau}\right)^2 \tag{A.7}$$
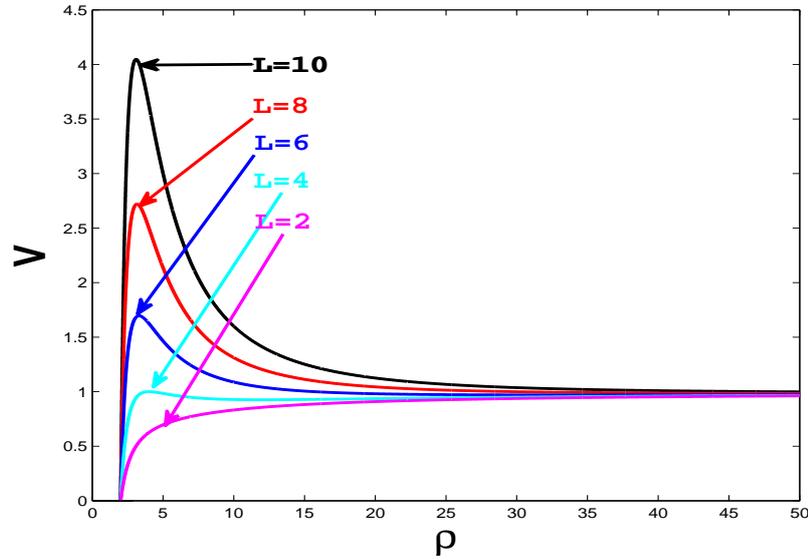
Figure A.1. The figure above shows the potential of the Schwarzschild spacetime.

so that

$$\left(\frac{dr}{d\phi}\right)^2 = \frac{r^4}{L^2}\left[E^2 - \left(1 - \frac{r_s}{r}\right)\left(\frac{L^2}{r^2} + 1\right)\right] \tag{A.8}$$

Exact solution to this equation is found in terms of elliptic integrals [76] and is given by

$$r = \frac{(1+e)\,r_1}{1 + e\cos\phi} \tag{A.9}$$

where r_1 is a root of the equation

$$\frac{dr}{d\phi} = 0 \tag{A.10}$$

and e the eccentricity parameter of the orbit.

Appendix B

Level Potential Plots

I this appendix I show two plots. The plot in the left panel is a function of the momentum L_z and the plot in the right panel is a function of the parameter δ.
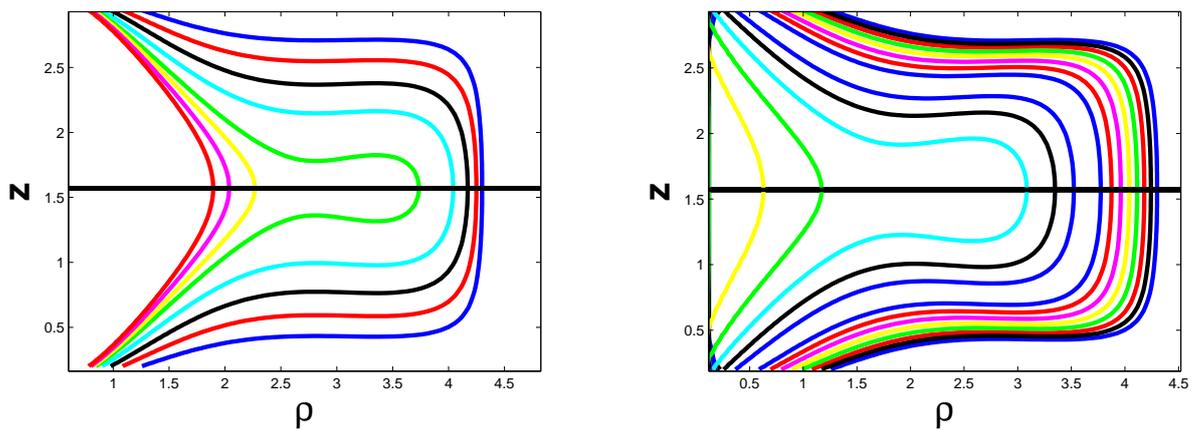
Figure B.1.   The first plot in the above figure shows level surfaces of the effective potential in the $\rho - z$ plane. As we increase the momentum L_z, the orbits get smaller. The second plot shows the potential as a function of decreasing δ.

Figure B.1 shows the effective potential in equation (4.7) as level plots in the $\rho - z$ plane. The first figure shows the potentials for increasing momentum from the highest potential to the lowest. Evidently the orbit shrinks as we increase the momentum which is expected for an object closer to a blackhole. The second figure

66

shows the potential with decreasing δ. For a fixed E and L_z, as we decrease δ, the orbit shrinks. This is a two dimensional way of visualizing the plots in figure 4.3 of section 4.1.

Appendix C

The Schwarzschild Metric as a limiting case of the Zipoy-Voorhees Spacetime $(\delta = 1)$

In this appendix, the appropriate transformation which reduces the Zipoy-Voorhees spacetime to the Schwarzschild spacetime for $\delta = 1$ is shown.

The Zipoy-Voorhees metric is given in equation (2.1). If we make the suitable change of coordinates

$$x = r - 1, \ y = cos\theta, \ z = \theta, \ \phi = \phi \tag{C.1}$$

Then the metric coefficients can be written as

$$
\begin{aligned}
e^{2\psi} &= \left(1 - \frac{2}{r}\right)^{\delta} \\
e^{2\gamma} &= \frac{\left(r^2 - 2r\right)^{\delta^2}}{\left(r^2 - 2r + sin^2\theta\right)^{\delta^2 - 1}} \\
\rho &= cosh^{-1}\left(r - 1\right)
\end{aligned}
\tag{C.2}
$$

so that

$$d\rho^2 = \frac{1}{(r^2 - 2r)} dr^2 \tag{C.3}$$

For $\delta = 1$ the metric (2.1) can be rewritten as

$$ds^2 = -\left(1 - \frac{2}{r}\right) dt^2 + \left(1 - \frac{2}{r}\right)^{-1} dr^2 + r^2 \left(d\theta^2 + sin^2\theta d\phi^2\right) \tag{C.4}$$

with $r_s = 2$ and thus we recover the Schwarzschild metric, in the special units where the mass, $M = 1$.

Appendix D

2-D Orbital pictures of the Zipoy-Voorhees Spacetime for Specified Parameter values

This appendix shows two figures (taken from the talk "YES, YES, YES, to describing particle orbits in SAV spacetimes" given by Jeandrew Brink, Caltech, 2009).

Figure D.1 show some orbital structures in the Zipoy-Voorhees spacetime for different initial conditions and with $E = 0.98$, $L_z = 7$. The first plot shows the case for $\delta = 3$. There are plunging orbits indicated by the blue and cyan curves and non plunging orbits as with the red. The second plot shows orbits for $\delta = 2$ and all orbits are nonplunging. The central black line approximates the centroid on the Poincaré map. The understanding of these plots is important in that it guides us how to specify the initial values Details and other features of such plots are discussed in section 4.1.
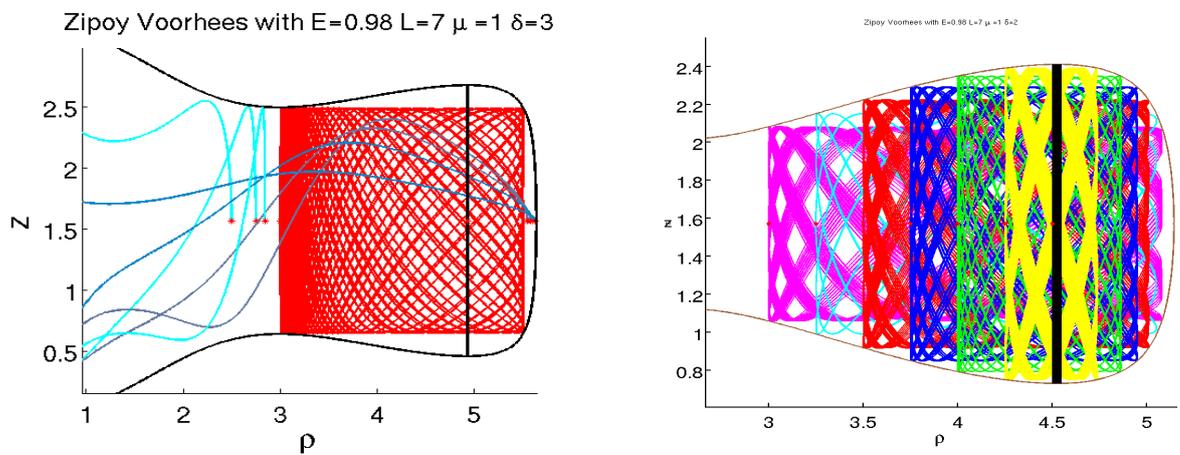
Figure D.1. The first plot in the above figure shows the orbits at different initial values in the $\rho - z$ plane. The blue and cyan curves are representative of plunging orbits while the red is nonplunging. The second plot shows all nonplunging orbits for $E = 0.98$ and $L_z = 7$ at different initial values. These pictures were taken from the talk "YES, YES, YES, to describing particle orbits in SAV spacetimes" given by Jeandrew Brink, Caltech, 2009.

Appendix E

Some Theory on the Curvature Tensor

This appendix reproduces some of the theory behind the curvature calculation methods mentioned in chapter 2. I start with an brief introduction to the curvature tensor and give the direct method which is in terms of coordinated [61,89]. In E.1.1 I discuss the Cartan structure equation which was the method used to compute the components of the curvature tensor obtained in equation (2.7).

E.1   The Curvature Tensor

We defne the curvature tensor as a map

$$\mathcal{R} : T\mathbf{M} \times T\mathbf{M} \times T\mathbf{M} \to T\mathbf{M} \tag{E.1}$$

given by the assignment

$$\mathcal{R}_{\mathbf{XY}}\mathbf{Z} = [\nabla_{\mathbf{X}}, \nabla_{\mathbf{Y}}] - \nabla_{[\mathbf{X},\mathbf{Y}]}\mathbf{Z} \tag{E.2}$$

for vector fields $\mathbf{X}$, $\mathbf{Y}$ and $\mathbf{Z}$.

It is not difficult to show that the value of $\mathcal{R}_{\mathbf{XY}}\mathbf{Z}$ depends only on the values of

the fields at some $p \in \mathbf{M}$.

Again as with the case of the torsion tensor, the formula is not very useful for calculations and to find a useful representation we choose fields associated with local coordinates defined in a neighbourhood.

$$
\begin{aligned}
\mathcal{R}_{\partial_i \partial_j} \partial_k &= \nabla_i \nabla_j \partial_k - \nabla_j \nabla_i \partial_k - [\partial_i, \partial_j] \partial_k \\
&= \nabla_i \left(\Gamma_{jk}^m \partial_m \right) - \nabla_j \left(\Gamma_{ik}^m \partial_m \right) \\
&= \partial_i \Gamma_{jk}^m \partial_m + \Gamma_{jk}^m \Gamma_{im}^c \partial_c - \partial_j \Gamma_{ik}^m \partial_m - \Gamma_{ik}^m \Gamma_{jm}^c \partial_c \qquad \text{(E.3)} \\
&= \left(\partial_i \Gamma_{jk}^m - \partial_j \Gamma_{ik}^m + \Gamma_{jk}^c \Gamma_{ic}^m - \Gamma_{ik}^c \Gamma_{jc}^m \right) \partial_m \\
&= \mathcal{R}_{kij}^m \partial_m
\end{aligned}
$$

where $\mathcal{R}_{kij}^m$ are the components of the curvature tensor (I refer the reader to [61] for a full reading on Riemann Curvature and the Lie Derivative). This equation happens to be a very straightforward way of computing our curvature tensor but a very computationally expensive one. An easier approach to computing the curvature lies with the Cartan's structure equations which I discuss in the next section.

E.1.1   Cartan's structure equations

I discuss the formalism behind behind the Cartan structure equations (this discussion ia adapted from [33]) which was used to find the components of the curvature tensor in (2.7). It is a less straightforward but very effective means of computing the components of the curvature tensor.

Choose some neighbourhood U on a manifold $\mathbf{M}$. Let $F = (F_1, ..., F_n)$ be an $n-$ *tuplet* of vector fields such that at each point $p \in U \subseteq \mathbf{M}$ the tuplet forms a basis of $T_p \mathbf{M}$. Then the collection $F = (F_1, ..., F_n)$ with the given property forms a "*frame field*". This is a generalization of how we choose $(\partial_1, ..., \partial_n)$ associated with chosen local coordinates $x^1, ..., x^n$ which defines the dual forms $(dx^1, ..., dx^n)$. The frame

field defines a dual collection of differential forms

$$\theta = \begin{pmatrix} \theta^1 \\ . \\ . \\ . \\ \theta^n \end{pmatrix} \tag{E.4}$$

such that $\theta\left(p\right)$ forms a dual basis.

A semi-Riemannian manifold $\mathbf{M}$ is a manifold is a manifold equipped with a nondegenerate symmetric $(0, 2)$ tensor field; (*i.e.*, $g : \mathbf{M} \to \mathbf{S}^2\left(T^*\mathbf{M}\right)$). An orthonormal frame field on a semi-Riemannian manifold $\mathbf{M}$ is one for which $(F_i, F_j){=}\epsilon_{ij}$ where

$$\begin{aligned} \epsilon_{ij} &= \pm 1 \quad for\ i = j \\ \epsilon_{ij} &= 0 \quad for\ i \neq j \end{aligned} \tag{E.5}$$

where (F_i, F_j) represents the inner product of F_i and F_j. Now, suppose $F{=}(F_i, ..., F_n)$ is an orthonormal frame field. Then $F\left(p\right)$ forms an orthonormal basis of $T_p\mathbf{M}$.

Take a tangent vector $v \in T_p\mathbf{M}$. The inner product of the vector with itself is given by

$$(v, v) = \epsilon_{11}\left(\theta^1\left(v\right)\right)^2 + ... + \epsilon_{nn}\left(\theta^n\left(v\right)\right)^2 \tag{E.6}$$

which is the metric (called the line element) and is usually simply written as

$$ds^2 = \epsilon_{11}\left(\theta^1\right)^2 + ... + \epsilon_{nn}\left(\theta^n\right)^2 \tag{E.7}$$

The First Structure Equation

I begin by stating two important identities: Suppose ω is a $0 - form$. Then

$$d\omega\left(\mathbf{X}\right) = \mathbf{X}\omega.$$

If ω is a $1 - form$ then

$$d\omega\left(\mathbf{X},\mathbf{Y}\right)=\tfrac{1}{2}\left(\mathbf{X}\omega\left(\mathbf{Y}\right)-\mathbf{Y}\omega\left(\mathbf{X}\right)-\omega[\mathbf{X},\mathbf{Y}]\right).$$

Define the linear differential form ω_j^i by

$$\omega_j^i\left(\xi\right)=\theta^i\left(\nabla_\xi F_j\right) \tag{E.8}$$

for some $\xi\in T_p\mathbf{M}$ such that

$$\nabla_\xi F_j=\omega_j^m\left(\xi\right)F_m.$$

Then

$$d\theta^i=-\omega_m^i\wedge\theta^m \tag{E.9}$$

or in a more compact form

$$d\theta=-\omega\wedge\theta \tag{E.10}$$

where $\wedge$ is the wedge product. The wedge product is antisymmetric and it is worth noting. That is,

$$\theta^m\wedge\omega_m^i=-\omega_m^i\wedge\theta^m$$

We should note that the antisymmetry would imply $\omega_i^i=0$. Either of equations (E.9) and (E.10) is known as the Cartan's first structure equations. It is fairly straightforward to prove by allowing both sides of the equation to act on a pair of elements from the frame field (F_r,F_s). That is, we are to show that

$$d\theta^i\left(F_r,F_s\right)=-\omega_m^i\wedge\theta^m\left(F_r,F_s\right)$$

I now proceed to verify.

$$d\theta^i\left(F_r,F_s\right)=F_r\theta^i\left(F_s\right)-F_s\theta^i\left(F_r\right)-\theta^i\left([F_r,F_s]\right) \tag{E.11}$$

$$=-\theta^i\left([F_r,F_s]\right) \tag{E.12}$$

For the R.H.S. of equation (E.11),

$$-\omega_m^i \wedge \theta^m (F_r, F_s) = \left(-\omega_m^i (F_r) \theta^m + \omega_m^i \theta^m (F_r) \right) (F_s) \qquad \text{(E.13)}$$

$$= -\omega_m^i (F_r) \theta^m (F_s) + \omega_r^i (F_s) \qquad \text{(E.14)}$$

$$= -\omega_s^i (F_r) + \omega_r^i (F_s) \qquad \text{(E.15)}$$

$$= -\theta^i \left(\nabla_{F_r} F_s - \nabla_{F_s} F_r \right) \qquad \text{(E.16)}$$

$$= -\theta^i \left([F_r, F_s] \right) \qquad \text{(E.17)}$$

and hence the proof.

The Cartan's first structure equation actually has an additional term which is the torsion $2 - form$ (represented by the torsion tensor). However, this term vanishes for a semi-Riemannian manifolds as the following theorem states:

Theorem E.1.1. *(Levi-Civita) Given any Semi-Riemannian Manifold* **M** *there exists a unique isometric connection* ∇ *which is torsion free.*

For a more indepth understanding of the subject I refer the reader to [33].

The second Structure Equation

We shall state the Cartan's second structure equation without proof. The proof follows as in the case for the first structure equation.

The second structure equation is given by

$$\Omega = d\omega_i^m + \omega_c^m \wedge \omega_i^c \qquad \text{(E.18)}$$

or simply

$$\Omega = d\omega + \omega \wedge \omega \qquad \text{(E.19)}$$

where Ω is related to the curvature tensor by

$$\Omega = \frac{1}{2} \mathcal{R}_{kij}^m \theta^i \wedge \theta^j \qquad \text{(E.20)}$$

Now that we have our set of equations, we outline the procedure for computing the curvature tensor from these equations.

- Determine the $1-forms$.

- We seek ω. We find these by computing $d\theta$ and comparing to equation (E.9).

- Find Ω.

- Write ω in terms of the wedge product over the $1-forms$ and compare to equation (E.20). See [61].

Bibliography

[1] The square kilometer array: Exploring the universe with the world's largest radio telescope. Accessed: 2016-09-23.

[2] B. Grammaticos A. Ramani and T. Bountis. The painlevé property and singularity analysis of integrable and non-integrable systems. Phys. Reports, 180(3):160–245, 1989.

[3] T. A. Apostolatos, G. Lukes-Gerakopoulos, and G. Contopoulos. How to observe a non - kerr spacetime using gravitational waves. Phys. Rev. Lett., 103(3):111101, 2009.

[4] B. Araneda and G. Dotti. arXiv, (1502.07153).

[5] V. I. Arnold. Russian Math. Survey, 18:85–193, 1963.

[6] Vladimir Igorevich Arnold. Mathematical methods of classical mechanics, volume 60. Springer Science & Business Media, 1989.

[7] I.M. Benn. Geodesics and killing tensors in mechanics. J. Math. Phys., 47:022903, 2006.

[8] George D. Birkhoff. Proof of Poincaré 's Geometric Theorem, volume 14. American Mathematical Society, 1913.

[9] George D. Birkhoff. Dynamical Systems, volume 9. American Mathematical Society, 1991.

[10] D. Boucher and W. Jacques-Arthur. Application of j. j. morales and j. p. and j. p. ramis theorem to teat the non-complete integrability of the planar three-body problem. IRMA Lectures in Mathematics and Theoretical Physics, 2003.

[11] Jeandrew Brink. Spacetime encodings ii. pictures of integrability. Phys. Rev. D., 78:102002, 2008.

[12] M. Brown and W. D. Neumann. Proof of the poincaré - birkhoff fixed point theorem. Michigan Math. J., 24, Jun. 1977.

[13] G. Calvert and N. M. J. Woodhouse. Painleve transcendents and einstein's equations. Class. Quant. Grav., 13:L33–L36, 1996.

[14] J. Carminati and R. G. McLenaghan. Algebraic invariants of the riemann tensor in a four-dimensional lorentzian space. Journal of Mathematical Physics, 32:3135–3140, Nov 1991.

[15] B. Carter. Axisymmetric blackhole has only two degrees of freedom. Phys. Rev. Lett., 26:331–333, 1971.

[16] N. A. Collins and S. A. Hughes. Phys. Rev. D., 69:124022, 2004.

[17] G. Contopoulos. Asymptotic curves and escapes in hamiltonian systems. Astronomy and Astrophysics, 231:41–55, 1990.

[18] André Deprit. Canonical transformations depending on a small parameter. Celestial Mechanics, 1:12–20, 1969.

[19] Robert L. Devaney. An Introduction to Chaotic Dynamical Systems. Westview Press, second edition edition, 2003.

[20] W. Y. Ding. A generalization of the poincaré-birkhoff theorem. Proceedings of the American Mathematical Society, pages 341–346, 1983.

[21] P. Dolan and B. D. Muratori. The lanczos potential for vacuum spacetimes with an ernst potential. JMP, 39(10), 1998.

[22] D. Petroff E. Barausse, L. Rezzolla and M. Ansorg. Phys. Rev. D, 75:064026, 2007.

[23] Frederick J Ernst. New formulation of axially symmetric gravitational field problem. Physical Review, 167:1175, 1968.

[24] F Dalbono-C F. D. C. Rebelo. Poincar e-birkhoff fixed point theorem and periodic solutions of asymptotically linear planar hamiltonian systems. Universitae Politecnico di Torino, page 233, 2002.

[25] M. Harsoula G. Contopoulos and G. Lukes-Gerakopoulos. arXiv, (1203.1010).

[26] T. A. Apostolatos G. Lukes-Gerakopoulos and G. Contopoulos. Phys. Rev. Lett, 103:111101, 2009.

[27] T. A. Apostolatos G. Lukes-Gerakopoulos and G. Contopoulos. Phys. Rev. D., 81:124005, 2010.

[28] T. A. Apostolatos G. Lukes-Gerakopoulos and G. Contopoulos. Int. J. Bifurc. Chaos, 21:2261, 2011.

[29] J. R. Gair and N. Yunes. Phys. Rev. D, 84:064016, 2011.

[30] Marisa Geyer. Geodesics and resonances of the manko-novikov spacetime. 2013.

[31] K. Glampedakis and S. Babak. Class. Quantum Gravity, 23:4167, 2006.

[32] Herbert Goldstein. Classical Mechanics. Addison-Wesley Publishing Company, 1980.

[33] P. Griffiths. On cartan's method of lie groups and iioving frames as applied to uniqueness and existence questions in differential geometry. 1974.

[34] Laurence S Hall. A theory of exact and approximate configurational invariants. Physica D, 8:90–116, 1983.

[35] B. Kent Harrison. Unification of ernst-equation backlund transformations using a modified wahlquist-estabrook technique. J. Math. Phys., 24:2178, 1983.

[36] Isidore Hauser and Frederick J. Ernst. Proof of a geroch conjecture. J. Math. Phys., 22(5):1051, 1981.

[37] S. W. Hawking. Blackholes in general relativity. Commun. Math. Phys., 25:152–156, 1972.

[38] Michel Hénon and Carl Heiles. The applicability of the third integral of motion: Some numerical experiments. Astron. J., 69:73–79, 1964.

[39] Jarmo Hietarinta. Direct methods for the search of the second invariant. Physics Reports, 147(2):87–154, 1987.

[40] Cornelius Hoenselaers. An approach to one killing-vector solutions of einstein's equations by rotation-coefficients. Progress of Theoretical Physics, 57(4):1223, 1977.

[41] W. Israel. Event horizon in static vacuum spacetimes. Phys. Rev., 164:1776–1779, 1967.

[42] M. Geyer J. Brink and T. Hinderer. The astrophysics of resonant orbits in the kerr metric. Phys. Rev. D., 91:083001, 2015.

[43] C. Li J. R. Gair and I. Mandel. Phys. Rev. D, 77:024035, 2008.

[44] W. M. Kinnersley. Type d gravitational fields. Ph.D. thesis, CALTECH, 1968.

[45] Christian Klein and Olaf Richter. Ernst Equation and Riemann Surfaces. Springer-Verlag Berlin Heidelberg, 2005.

[46] Horst Knörrer. Geodesics on the ellipsoid. Inventiones math., 59:119–143, 1980.

[47] Hideo Kodama and Wataru Hikida. Zipoy - voorhees - weyl spacetime and the δ= 2 tomimatsu - sato spacetime. Class. Quantum Gravity, 20:5121–5140, 2003.

[48] A. N. Kolmogorov. On preservation of conditionally periodic motions under a small change in the hamiltonian function. In Dokl. Akad. Nauk SSSR, volume 98, pages 527–530, 1954.

[49] F. M. Paiva L. Herrera and N. O. Santos. The levi-civita space–time as a limiting case of the γ space–time. J. Math. Phys., 40:4064, 1999.

[50] F. M. Paiva L. Herrera and N. O. Santos. The levi-civita space–time as a limiting case of the γ space–time. Journal of Mathematical Physics, 40(8):4064–4071, 1999.

[51] R. E. Langer. The solutions of the mathieu equation with a complex variable and at least one parameter large. Transactions of the American Mathematical Society, 36(3):637–695, 1934.

[52] Jean Leray. Hyperbolic Differential Equations. reprinted november 1955 edition, 1953.

[53] G. Lukes-Gerakopoulos. arXiv, (1206.0660).

[54] Andrzej J Maciejewski, Maria Przybylska, and Tomasz Stachowiak. Nonexistence of the final first integral in the zipoy-voorhees space-time. Physical Review D, 88(6):064003, 2013.

[55] KB Marathe. On the petrov classification of orthogonal metric-spaces. Proceedings of the National Institute of Sciences of India: Physical sciences, 34:301, 1968.

[56] P. W. Michor and D. Mumford. An overview of the riemannian metrics on spaces of curves using the hamiltonian approach. Applied and Computational Harmonic Analysis, 23:74–113, 2007.

[57] C.W. Misner, K.S. Thorne, and J.A. Wheeler. Gravitation. Freeman: San Francisco, 1973.

[58] J. J. Morales-Ruiz and J. P. Ramis. Integrability of dynamical systems through differential galois theory: A practical guide. AMS, 2009.

[59] Nikolai Nikolaevich N. N. Nekhoroshev. The poincaréâĂŤlyapunovâĂŤliouvilleâĂŤarnol'd theorem. Functional Analysis and Its Applications, 28(2):128–129, 1994.

[60] Zbigniew Nitecki. Differentiable dynamics. MIT press, 1971.

[61] B. O'neill. Semi-Riemannian Geometry With Applications to Relativity, 103, volume 103. Academic press, 1983.

[62] Demetrios Papadopoulos, Bob Stewart, and Louis Witten. Some properties of a particular static, axially symmetric space-time. Phys. Rev. D., 24(2):320, 1981.

[63] R Pavani. The numerical approximation of the rotation number of planar maps. Computers & Mathematics with Applications, 33(5):103–110, 1997.

[64] Roger Penrose and Malcolm AH MacCallum. Twistor theory: an approach to the quantisation of fields and space-time. Physics Reports, 6(4):241–315, 1973.

[65] Aleksey Zinovjevitch Petrov. The classification of spaces defining gravitational fields. Uchenye Zapiski Kazanskogo Gosudarstvennogo Universiteta im. VI Ulyanovicha-Lenina [Scientific Proceedings of Kazan State University, named after VI Ulyanov-Lenin], 114,(8) 55-69 (1954)). Jubilee (1804-1954) Collection., 114:55–69, 1954.

[66] Jules Henri Poincaré. Sur le probléme des trois corps et les Ãŋquations de la dynamique. divergence des sÃŋries de m. lindstedt. Acta Mathematica, 13:1–270, 1890.

[67] Jürgen Pöschen. A lecture on the classical kam theorem. Proc. Symp. Pure Math, 9(69):707 – 732, 2001.

[68] E.G. Poznyak and E.V. Shinkin. Origin of problems in the theory of surfaces of negative curvature (survey of work up to 1950). J. Sov. Math., 5:865–87, 1976.

[69] W.H. Press, S.A. Teukolsky, W.T. Vetterling, and B.P. Flannery. Numerical Recipes in C++. Cambridge University Press, second edition, 2002.

[70] J. D.Farmer R. E. Ecke and D. K. Umberger. Scaling of the arnold tongues. Nonlinearity, 2(2):175, 1989.

[71] J. Casanellas et. al R. P. Eatough, T. J. W. Lazio. Observing radio pulsars in the galactic center with the square kilometer array. arXiv, (1501.00281v1).

[72] C. Rebelo. A note on the poincaréâĂŤbirkhoff fixed point theorem and periodic solutions of planar systems. Nonlinear Analysis: Theory, Methods & Applications, 29(3):291–311, 1997.

[73] C. Robinson. Uniqueness of the kerr blackhole. Phys. Rev. Lett., 34:905–906, 1975.

[74] F. D. Ryan. Phys. Rev. D., 52:5707, 1995.

[75] N. Yunes S. J. Vigeland and L. C. Stein. Phys. Rev. D, 83:104027, 2011.

[76] Gunter Scharf. Schwarzschild geodesics in terms of elliptic functions and the related red shift. arXiv preprint arXiv:1101.1207, 2011.

[77] Heinz Georg Schuster and Wolfram Just. Deterministic Chaos, An Introduction. Wiley - VCH Verlag GmbH & and Co. KGaA, 2005.

[78] Bernard F. Schutz. Geometrical methods of mathematical physics. Cambridge Univeristy Press, 1980.

[79] Hans Stephani, Dietrich Kramer, Malcolm Maccallum, Cornelius Hoenselaers, and Eduard Herlt. Exact Solutions of Einstein's Field Equations. Cambridge University Press, 2nd edition, 2003.

[80] Steven H. Strogatz. Nonlinear Dynamics and Chaos with applications to Physics, Biology and Chemistry and Engineering. Perseus Books, 1994.

[81] Victor Szebehely. Theory of orbits: The restricted three body problem. Soviet Astronomy, 13(2), 1969.

[82] Michael Tabor. Chaos and Integrability in nonlinear Dynamics. John Wiley & Sons Inc., 1989.

[83] Micheal E. Taylor. Partial Differential Equations III- Nonlinear Equations. Springer Verlag, 1996.

[84] L. W. Tu. An Introduction to Manifolds: Second Edition. Springer, 2011.

[85] V.S. Vladimirov. Equations of Mathematical Physics. Marcel Dekker Inc. 95 Madison Ave. New York 10016, 1971.

[86] V.S. Vladimirov. A Collection of Problems on the Equations of Mathematical Physics. Springer-Verlag, New York, 1986.

[87] B.H. Voorhees. Static axially symmetric gravitational fields. Phys. Rev. D, 2(10):2119, 1970.

[88] R. Wald. Construction of solutions of gravitational, electromagnetic, or other perturbation equations from solutions of decoupled equations. Phys. Rev. Lett., 41:203–6, 1978.

[89] Robert M. Wald. General Relativity. The University of Chicago Press, 1984.

[90] Martin Walker and Roger Penrose. On quadratic first integrals of the geodesic equations for type 22 spacetimes. Commun. Math. Phys, 18:265–274, 1970.

[91] Eric W. Weisstein. Kolmogorov-arnold-moser theorem from mathworld–a wolfram web resource.

[92] Eric W. Weisstein. Rotation number from mathworld: A wolfram web resource.

[93] K. J. Whiteman. Invariants and stability in classical mechanics. Rep. Prog. Phys., 40:1033 – 1069, April 1977.

[94] E.T. Whittaker. A Treatize on the Analytical Dynamics of particles and rigid bodies. New York Dover Publications, 1944.

[95] N. M. J. Woodhouse. Killing tensors and the separation of the hamilton-jacobi equation. Commun. Math. Phys, 44:9–38, 1975.

[96] Basilis C. Xanthopoulos. Integrals of motion and analytic functions. J. Phys. A: Math. Gen, 17:87–94, 1984.

[97] Basilis C. Xanthopoulos. Symmetries and solutions of the einstein equations. Geometric Aspects of the Einstein Equations and Integrable Systems, 239:77–107, 1984.

[98] D. M. Zipoy. Topology of some spherioidal metrics. J. Math. Phys., 7:1137, 1966.